LATVIAN JOURNAL of PHYSICS and TECHNICAL SCIENCES

ISSN 0868 - 8257

5

(Vol. 59)

2022

CONTENTS

LATVIAN JOURNAL of PHYSICS and TECHNICAL SCIENCES

LATVIJAS FIZIKAS un TEHNISKO ZINĀTŅU ŽURNĀLS

ЛАТВИЙСКИЙ ФИЗИКО-ТЕХНИЧЕСКИЙ ЖУРНАЛ

Published six times a year since February 1964
Iznāk sešas reizes gadā kopš 1964. gada februāra
Выходит шесть раз в год с февраля 1964 года

5 (Vol. 59) • 2022

RĪGA

Language Editor: O. Ivanova
Computer Designer: I. Begicevs

INDEXED (PUBLISHED) IN

www.scopus.com
www.sciendo.com
EBSCO (Academic Search Complete, www.epnet.com), INSPEC (www.iee.org.com).
VINITI (www.viniti.ru), Begell House Inc/ (EDC, www.edata-center.com).

Issuers: Institute of Physical Energetics,
Institute of Solid State Physics, University of Latvia
Registration Certificate Number: 000700221

Editorial Contacts:
14 Dzerbenes Street, Riga, LV - 1006
Ph.: + 371 67551732
E-mail: leo@lza.lv
www.fei-web.lv

sciendo

LATVIAN JOURNAL OF PHYSICS
AND TECHNICAL SCIENCES
2022, N 5

DOI: 10.2478/lpts-2022-0036

FIBRE OPTICAL COUPLER SIMULATION BY COMSOL MULTIPHYSICS SOFTWARE

E. Elsts[1*], A. Supe[2], S. Spolitis[2], K. Zakis[2], S. Olonkins[3],
A. Udalcovs[2], R. Murnieks[2], U. Senkans[2], D. Prigunovs[2,3],
L. Gegere[2,3], K. Draguns[4], I. Lukosevics[1], O. Ozolins[2],
J. Grube[1], V. Bobrovs[2]

[1]Institute of Solid State Physics, University of Latvia,
8 Kengaraga Str., Riga, LV-1063, LATVIA
[2]Institute of Telecommunications, Riga Technical University,
12 Azenes Str., Riga, LV-1048, LATVIA
[3]AFFOC Solutions,
2-58 Jaunibas Str., Kalnciems, LV-3016, LATVIA
[4]Institute of Atomic Physics and Spectroscopy, University of Latvia,
3 Jelgavas Str. - House of Science, Riga, LV-1004, LATVIA
*e-mail: edgars.elsts@cfi.lu.lv

The paper presents a simulation model developed for a special optical coupler intended for coupling radiation from signal and pump sources used for the realization of cladding-pumped doped fibre amplifiers. The model is developed in COMSOL Multiphysics and used to assess the pumping efficiency for different side pumping angles and different numbers of electromagnetic modes. The obtained results show that the highest pumping efficiency, above 75 %, is achieved for 5–14 modes when two fibres representing the pump source and the signal source form a 10-degree angle between their central axes. The search for the optimal number of modes corresponds to the development trend in optical coupler technology where the multimode pumping by light-emitting diode (LED) replaces the classical scheme with a single-mode pumping by a laser diode (LD).

Keywords: *COMSOL MULTIPHYSICS, double-clad fibre, optical coupler, side pumping*.

1. INTRODUCTION

Recently, cladding-pumped doped fibre amplifiers have attracted interest for application in space-division multiplexed (SDM) systems proving a transmission capacity increase in a cost-effective way [1], [2]. Hence, an appropriate amplifier is required for signal transmission over long distances (>100 km).

The most widely used optical amplifiers in telecommunications are the Erbium-Doped Fibre Amplifiers (EDFAs) and RAMAN effect based amplifiers. Optical signal amplification beyond optical C and L bands using doped fibre amplifiers is possible with other trivalent rare earth elements (ytterbium, thulium, neodymium, holmium, etc.) and their combinations. Co-doped fibre-based amplifiers are very promising solutions due to their low nonlinearity without degrading amplification efficiency [3]. For example, erbium combination with ytterbium allows increasing the distance between the erbium ions in the amplifying medium; therefore, co-doping with erbium/ytterbium minimizes the possibility of clustering of erbium, allowing for a higher concentration of erbium in the amplifying medium compared to the conventional implementation of erbium-doped fibres. As a result, shorter erbium/ytterbium-doped fibres are required to achieve a similar level of gain [4]. While for the Raman amplifiers pumping can be performed at any wavelength (i.e., there is no absorption band), and the signal characteristics are determined by optical phonon spectra in contrast to the rare-earth-doped fibre amplifiers, where the pump characteristics and signal bands are fixed [5].

The cladding pumping technique differs from the classic approach where pump light is coupled directly in the doped fibre core. Instead, high-power pump radiation is launched into a much larger inner cladding of double-cladding fibre. The pump light propagation regime in the inner cladding is highly multi-modal and therefore has a high probability of repeatedly crossing the core of double-cladding fibre. Once the pump reaches the core it is absorbed gradually by dopant ions, while the signal amplification process is the same as in the case of core pumping [6].

The key to optimal cladding-pumping performance is special double-clad fibre couplers [7]. These couplers ensure that signal is coupled into the output fibre core, but the pump light is guided into the inner cladding. Regarding cladding-pumping couplers, there are several possible realizations, for example, free space coupling (end pumping), tapered fibre bundles, geometrically multiplexed end-pumping, V-groove side pumping, shallow-angle side pumping, etc. For further studies, a shallow-angle side pumping scheme was chosen because of good characteristics in terms of efficiency, preservation of modal properties, and robust construction [8].

In addition to long-distance telecommunication networks, fibre optic couplers are used in various other areas, such as optical sensors in biophotonics [9], [10], combined optical coherence tomography and hyperspectral imaging in medicine [11], free-space optical communications [12], etc. Optimum performance of optical fibre amplifiers is also determined by the optical composition of optical fibres and their resistance to harsh environmental conditions [13]–[17].

An optical fibre amplifier consists of a doped fibre, one or more pump lasers, a passive wavelength coupler, which is also the

focus of this paper, optical isolators (Bragg grating (FBG) or Faraday rotator), and tap couplers (Fig. 1). The pump light is inserted into the rare-earth-doped fibre through a wavelength selective coupler where these schemes can be forward pumping (co-pumped), backwards-pumping (counter-pumped), or bidirectional-pumping (dual-pumped) [18], [19].

In forward pumping, the input signal and the pump signal propagate in the same direction inside the fibre; in back-pumping, the input signal and the pump signal propagate in opposite directions. Bidirectional pumping is performed in both directions simultaneously (Fig.1).

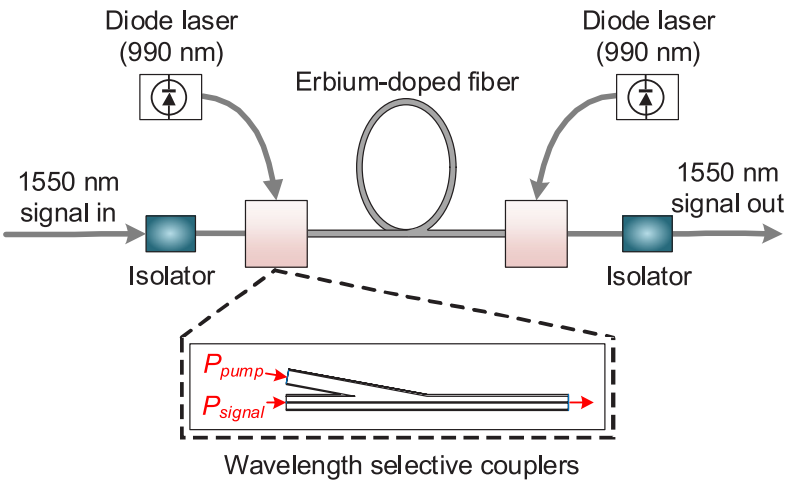

Fig. 1. Configuration of rare-earth-doped fibre amplifier employing a bidirectional pumping scheme.

Coupling efficiency is one of the most significant parameters that characterises a coupler. Because not all of the light from the pumping fibre is transferred to the information-carrying double-clad fiber. Coupling efficiency in fibre optics is the efficiency of optical power transfer between two optical components such as two optical fibres. Coupling efficiency is usually expressed as the ratio of output power to input power, converted to per cent [20], [21].

Coupling efficiency is determined by factors such as the optimal number of electromagnetic modes, the optimal angle between pumping and information-carrying fibres, etc. To the best of our attempt, no information was found about other studies performed by the COMSOL Multiphysics Software simulating the influence on coupler performance of these parameters.

The angle-polished method is efficient to connect pumping and information-carrying fibres. The efficiency of the coupler has been modelled by geometric optical methods analysing the light transmission in the core and inner cladding and the loss in the boundary between the inner and outer cladding of the double-clad fiber [22]. Multimode interference improves pumping efficiency through the reimaging effect to prevent light from diverging when exiting the fibre [23], [24].

Therefore, in this study, the number of electromagnetic modes is varied to find out at which number of modes the coupler reaches the highest efficiency.

For multimode pump fibre, to calculate coupling efficiency η_{lat} formulas [25], [26] could be applied. Lateral coupling efficiency is given by the formula:

$$\eta_{lat} \simeq \frac{16(n_1/n)^2}{[1+(n_1/n)^4}\frac{1}{\pi}\left\{2\cos^{-1}\left(\frac{y}{2a}\right)-\left(\frac{y}{a}\right)\left[1-\left(\frac{y}{2a}\right)^2\right]^{\frac{1}{2}}\right\}, \quad (1)$$

where n_1 is the refractive index of the core, n is the medium refractive index among the fibres, y is the lateral displacement of the axes of the fibre core and a is the radius of the fibre core.

Angular coupling efficiency is given by the formula:

$$\eta_{ang} \simeq \frac{16(n_1/n)^2}{[1+(n_1/n)]^4}\left[1-\frac{n\theta}{\pi n_1(2\Delta)^{\frac{1}{2}}}\right], \quad (2)$$

where Θ is the angular displacement in radians and Δ is the relative difference between the refractive indices of the fibre. The insertion loss due to angular misalignment may be obtained from the angular coupling efficiency in the same manner as the lateral misalignment loss following.

To combine multi-mode and single-mode fibre, a more complex simulation technique must be used for simulations. The most commonly used techniques are summarised below:

- In the effective-index method, a two-dimensional coupler structure is converted into an equivalent one-dimensional slab problem [27].
- The step-approximation method (Burns' method), where the amplitude transmission and mode conversion coefficients for the even and odd normal modes across the steps are rigorously obtained taking into account the phase difference between the two normal modes [28], [29].
- The finite-difference beam-propagation method (BPM) is a widely used algorithm for the solution of Maxwell's equations. It is applied to the eigenmode, propagating beam, and time-domain analyses of optical waveguides [30], [31].
- Finite Element Method (FEM) is a numerical technique that gives approximate solutions to differential equations that model problems arising in physics and engineering. As with the more commonly used finite difference schemes, the finite element method reduces problems defined in geometrical space (or domain) to find a solution in a finite number of points by subdividing the domain into smaller regions (a mesh) [32].

Further, the results of other authors who performed simulations similar to ours using the COMSOL Multiphysics software package are briefly described.

A coupling mechanism of a photoconductive terahertz antenna with radial symmetry was presented in [33]. The 3-D simulation domain is discretized into approximately 1.8 million tetrahedral mesh elements yielding a computational model consisting of 2.1 million degrees of freedom. The cylinder (2 cm diameter, 4 cm length) is placed such that its central axis lies at the centre of the gap between the waveguide and coupler wires. Part of the cylinder extends outside of the rectangular box, for a waveguide 15 cm long. The coupling efficiency of the scattering mechanism was 56 %–50 %.

The coupling efficiency was analysed [34] between the antenna and waveguide The excitation of gap plasmon waveguide (GPW) by dipole nanoantenna was simulated and results were compared with corresponding predictions obtained using standard antenna theory. The minimum mesh size was set to 3 nm. The size of the computational domain was always

3 μm × 3 μm × 3.5 μm. It was found that the use of nanoantennas could increase the conversion of an incident beam into a waveguide mode dramatically.

Non-volatile phase change materials (PCM) – clad silicon photonic 1 × 2 and 2 × 2 switches –, which can be used for applications such as optical interconnects, neuromorphic computing, quantum computing, and microwave photonics, were demonstrated [35]. The grid size of the mesh in our simulation was set at 20 nm in dimensions. A study was performed on how to improve the efficiency of the coupler.

In [36], a technique for the highly stable and efficient generation of radially TM01 and azimuthally TE01 polarized beams using weakly-fused fibre couplers was investigated. Based on the above analysis and the simulations shown, a conventional telecom-grade SMF (Elliot Scientific, SMF-1300/1500 core/cladding diameter = 8.2/125 μm, NA = 0.14) was adiabatically pre-tapered at ∼1400 ºC to a radius of r ∼ 38.6±0.1 μm for exciting the TE01 mode (NTT-AT, Japan). The fundamental mode in the SMF is directly coupled to the TM01 or TE01 mode by appropriately phase matching the modes in the fibres resulting in an efficiency of ∼67 % and ∼85 %, and polarization purity of 70 % and 82 %, respectively.

Optical waves confined within high refractive index regions if flanked by adjacent low index regions for biological event monitoring were studied [37]. To obtain converged results, a 0.2 mm maximum mesh size in the piezoelectric material region, a 0.15 mm maximum mesh size in the cavity, and a 1 mm mesh size in the Perfectly Matched Layer (PML) region were used. Each imagined sample was 100 μm to quantify the extent and depth of optical confinement in the cylindrical cavity (19 mm radius, 30 mm height). The input beam can be optimized to match the NA and maximize the coupling efficiency.

In the scheme presented by [38], a tapered nanofibre (TNF) was evanescently coupled with a substrate, allowing the pump light guided in the TNF to generate a strong transverse optical force for the light-control-light effect. The mesh sizes of the tapered nanofiber (TNF) and medium were 5 nm and 50 nm. The calculation space for the simulation was set as 7 μm × 9 μm × 60 μm and a TNF with a length of 60 μm was located at the centre of the calculation region along the z-direction.

In the study covered by this paper, based on data summarised in the above-mentioned publications, the numerical simulations of side coupling injection with the aid of COMSOL Multiphysics were performed to analyse its efficiency.

The rest of the manuscript is structured as follows: Section II describes the simulation methodology and input parameters of the modelled coupler as well as the obtained results. Finally, Section III provides a summary of the simulated results and concludes the paper.

2. METHODS AND RESULTS

The design of the coupler was simulated by COMSOL Multiphysics software using a two-dimensional model [39].

The 2D model was chosen as suitable because it required fewer computer resources and provided sufficient quality compared to the 3D model.

Electromagnetic field simulations were

performed using the Wave Optics Module of the software. The workflow can be described by the following steps:

- define the geometry;
- select materials;
- select a suitable Wave Optics interface;
- define the boundary and initial conditions;
- define the finite element mesh;
- select a solver;
- visualize the results.

To obtain characteristic values for calculating the electric and magnetic fields of the coupler, COMSOL Multiphysics built-in function *line integration* was used. This function evaluates a *line integration* value over the cut line in models of an electric and magnetic field. *Line integration* is expressed as the variable *normE,* which represents the amplitude of the electric field, and variable *normH,* which represents the amplitude of the magnetic field, respectively.

To describe the propagation of light in an optical fibre, power flow was examined using the time-averaged Poynting vector, which is the cross product of the electric field and the magnetic field:

$$\boldsymbol{S} = \frac{1}{2} Re(\boldsymbol{E} \times \boldsymbol{H}). \quad (3)$$

The studied coupler (shown in Fig. 2) has an information-carrying fibre (A) and pumping fibre (B) connected at an angle *g*, and a tapered section (C). Information-carrying fibre consists of single-mode (SM) core, an inner cladding, and an outer cladding. The pump fibre, respectively, consists of a multimode (MM) core and an outer cladding. Simulation parameters are given in Table 1.

Tab. 1. Fibre Parameters Used in our Simulations

Input and output fibre			**Pump fibre**		
Purpose	Diameter (μm)	Refractive index	Purpose	Diameter (μm)	Refractive index
SM core	5.8	1.5431	MM core	105	1.5293
SM inner cladding	105	1.5293	MM outside cladding	125	1.5054
SM outside cladding	125	1.5054			

The refractive indices of the core and claddings of the above-mentioned fibres were determined from commercially available double-cladding fibre with flower-shaped inner cladding. Scanning electron microscope (SEM) results of double cladding fibre showed the presence of phosphorus in the fibre core, which increased the refractive index of silica, the inner cladding was silica without any traces of rare-earth or additional dopant elements, and the outer cladding was made of fluorine-doped silica to reduce the refractive index of the material.

In our model, the length of information-carrying optical fibre is 2.25 mm and a pump fibre length is 1.12 mm. The reason for choosing such dimensions is the trade-off between the ability to easily monitor the model by software and the calculation time. The functional scheme of the coupler model is shown in Fig. 2.

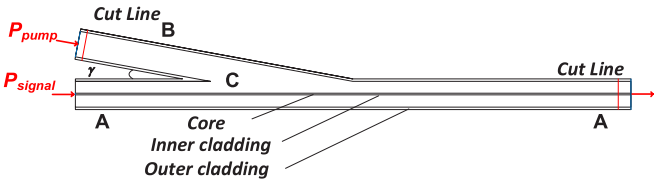

Fig. 2. Functional scheme of the coupler (information-carrying SM optical fibre (A) and pumping MM fibre (B) connected at an angle *g*, a tapered section (C), red-coloured cut lines indicate the location for line integration calculation).

The information-carrying optical signal is modelled taking into account an expected optical signal power: P_{sign}>1 mW at wavelength λ_{sign}=1550 nm and a pumping signal with power: P_{pump}=3W at wavelength λ_{pump}=980 nm.

The finite element method (FEM) is mesh-dependent, which means smaller elements can provide better representation. The finite element mesh is used to subdivide the model into smaller domains called elements, over which a set of equations is solved.

In our models, the mesh type was selected as "boundary layers", which was characterised by a dense distribution of elements in the normal direction along specific boundaries. Element size parameters – maximum element size: 2.25 μm, minimum element size: 0.225 μm, maximum element growth rate: 1.08, curvature factor: 0.25, and resolution of narrow regions: 1. This is a compromise between calculation quality and calculation time.

In our initial simulation, the signal with P_{sign}>1 mW at wavelength λ_{sign}=1550 nm was injected only in single-mode optical fibre (Fig. 3).

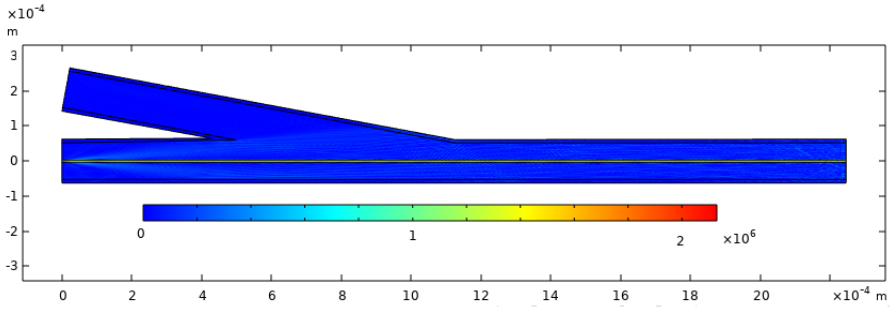

Fig. 3. The simulation of the signal propagating through the coupler (single-mode fibre core). Colours correspond to the strength of the electromagnetic field.

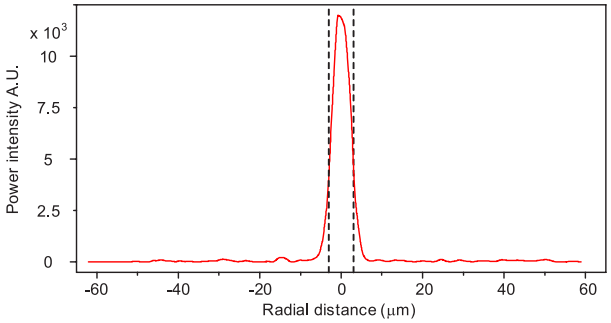

Fig. 4. A section of single-mode signal fibre shows an increase in intensity at the core of the fibre. Black dashed lines indicate fibre core diameter.

As shown in Fig. 3, the colour of the core is closer to red, indicating a more intense signal, and the other parts are blue, indicating the absence of signal. Figure 4 shows the electromagnetic field intensity dependence on the radial distance from the centre. The electromagnetic field intensity is represented by a red solid line, and the core diameter (5.8 μm) is represented by black dashed lines. The strongest signal is in the core of the fibre and a transitional region is observable on the border between core and cladding. *Cut line* locates at a distance of $16 \cdot 10^{-4}$ m from the beginning of the double cladding fibre (after connection pumping and signal fibres). Signal parameters in single-mode fibre do not change significantly as the signal propagates.

The part of the single-mode fibre that carries most of the light energy is larger than the core diameter of this fibre (Fig. 4). This phenomenon is called the mode field diameter (MFD). The MDF depends on the wavelength, the radius of the core, and the indices of refraction of the core and the cladding. The signal can be approximated by a Gaussian power distribution.

The next step in our simulations is the injection of the pumping signal with the power P_{pump}=3 W at wavelength λ_{pump}=980 nm into a multimode fibre.

The pump efficiency was analysed as a function of the connection angle between pumping fibre and the signal fibre at angles of 5°, 10°, 20° and 30°.

A 10-mode pumping signal was used. At an angle of 5°–10° coupler efficiency is about 95 %, but as the angle increases to 20°–30° degrees, the efficiency decreases rapidly to 2–5 %. The model with a 10° angle between the signal and the pumping fibre (Fig. 2) is found to be optimal because at a smaller angle the pumping signal tends to propagate backwards.

The optimal coupling angle of 5º–10º calculated by COMSOL Multiphysics agrees with the angle of 10º published in [40], where calculations were done using geometric optics with a step of 0.5 º and proved experimentally.

The dependence of the coupler efficiency on the number of modes injected into the double-cladding multimode pumping fibre was modelled in our study.

Coupling efficiency was assumed as the ratio of the power near the beginning of multimode pumping fibre, which was coupled into a single-mode double-clad fiber, and power registered near the end of double-clad fiber (see red-coloured *cut lines* in Fig. 2). *The line integration* function was used for numerical estimation.

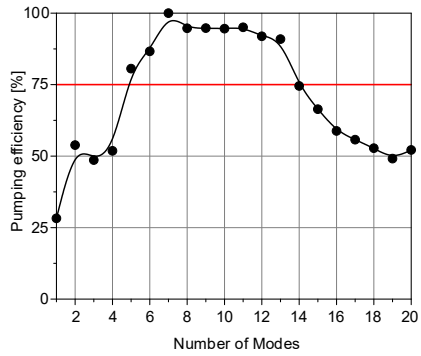

Fig. 5. Dependence of coupler efficiency on the number of electromagnetic modes.

The simulation shows the highest pumping efficiency with 7 electromagnetic modes, but it should be noted that the results would be more representative if the fibres were longer, but it would take more time to run such simulations.

The range of 5 to 14 electromagnetic modes was considered the most suitable, with an efficiency of over 75 %, as represented in Fig. 5. For instance, for the 50-mode model, only ~10 % pump efficiency can be achieved.

The power of the high-order modes leaks more than the power of low-order modes [41]–[43].

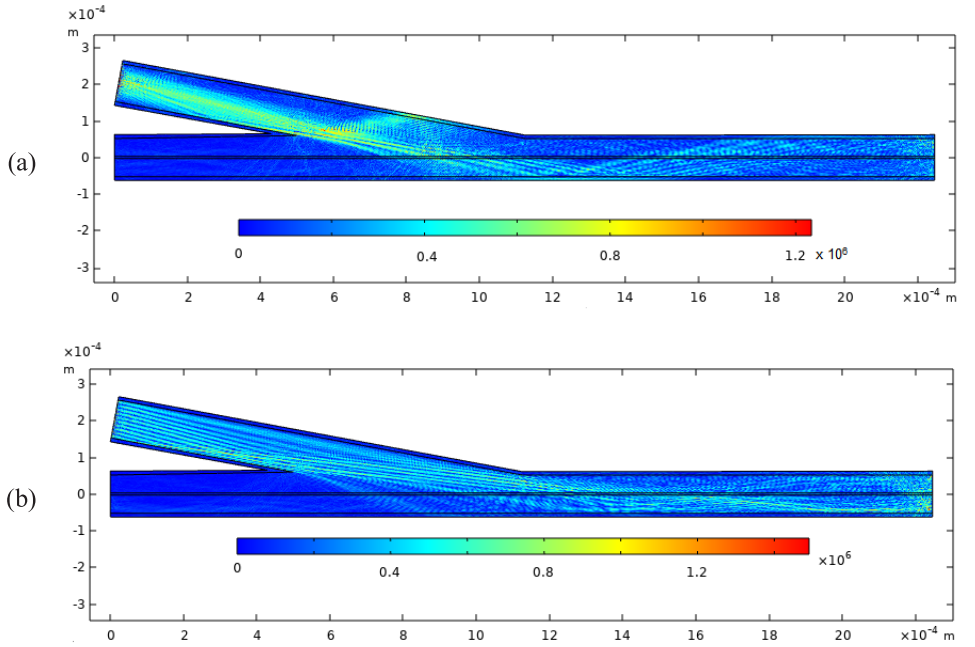

Fig. 6. The 2-dimensional coupler model in COMSOL Multiphysics forms a 10º angle between the pumping and the signal-carrying fibre with one (a) and ten (b) electromagnetic modes injected in the pumping fibre.

In Fig. 6, for illustration, one (a) and ten (b) modes are injected into a multimode pump fibre. The pump signal initially propagates almost parallel to the direction of the fibre, but entering the double-clad fibre starts to reflect from the outer coating. This pump signal propagation behaviour remains true in models with different number of modes which were calculated but not featured in this article.

In the research [44], the coupling efficiency as a function of the number of pumping modes was analysed using experimental data and Finite Difference Beam Propagation Method (FD-BPM) simulations. Pronounced peaks corresponding to 3 and 10 modes were observed, corresponding to multimode fibres with radii of 52.5 and 92.5 μm, respectively. That means the simulation model works correctly and our results are close to the already validated results. Note that recent overview of the current status of fibre-based multimode interference (MMI) devices with a particular focus on optical fibre-based sensing applications was presented in [45].

3. CONCLUSIONS

In this paper, an overview of couplers as an important component of amplifiers in optical communications networks was presented and useful results from the literature for coupler modelling with COMSOL Multiphysics software package were summarised.

A successful two-dimensional model simulating electric and magnetic fields in coupler with COMSOL Multiphysics software was developed, which showed that the optimum number of pumping modes lied in the range of 5 to 14 modes, which was similar to the previously reported results

but obtained by different methods.

The developed simulation methodology is an important step forward in the studies of optical couplers using the COMSOL Multiphysics environment. However, to test our simulation results experimentally the mode-filtering technique has to be applied. To accurately distinguish leakage from uncontrolled backward propagation additional experiments using FBG or Faraday rotation filters could be applied.

ACKNOWLEDGEMENTS

Funding: The research has been supported by the European Regional Development Fund project No.1.1.1.1/18/A/068.

The Institute of Solid State Physics, University of Latvia as a Center of Excellence has received funding from the European Union's Horizon 2020 Framework Programme H2020-WIDESPREAD-01-2016-2017-TeamingPhase2 under grant agreement No. 739508, project CAMART2.

REFERENCES

1. Puttnam, B. J., Rademacher, G., & Luís, R. S. (2021). Space-Division Multiplexing for Optical Fibre Communications. *Optica*, *8* (9), 1186–1203.
2. Yoshikane, N., & Tsuritani, T. (2020). Recent progress in space-division multiplexing optical network technology. In: *2020 International Conference on Optical Network Design and Modeling (ONDM)* (pp. 1–4). 18–21 May 2020, Barcelona, Spain, IEEE.
3. Aiso, K., Tashiro, Y., Suzuki, T., & Yagi, T. (2001). Development of Er/Yb Co-doped Fibre for High-Power Optical Amplifiers. *Furukawa Electric Review*, 35–39.
4. Supe, A., Olonkins, S., Udalcovs, A., Senkans, U., Mūrnieks, R., Gegere, L., … & Bobrovs, V. (2021). Cladding-Pumped Erbium/Ytterbium Co-Doped Fibre Amplifier for C-Band Operation in Optical Networks. *Applied Sciences*, *11* (4), 1702.
5. Selvarajan, A., Kar, S., & Srinivas, T. (2003). *Optical Fibre Communication: Principles and Systems*. Tata McGraw-Hill Education.
6. Filippov, V., Kerttula, J., Chamorovskii, Y., Golant, K., & Okhotnikov, O. G. (2010). Highly Efficient 750 W Tapered Double-Clad Ytterbium Fibre Laser. *Optics Express*, *18* (12), 12499–12512.
7. Lei, C., Chen, Z., Leng, J., Gu, Y., & Hou, J. (2017). The Influence of Fused Depth on the Side-Pumping Combiner for All-Fibre Lasers and Amplifiers. *Journal of Lightwave Technology*, *35* (10), 1922–1928.
8. Supe, A., Spolitis, S., Elsts, E., Murnieks, R., Doke, G., Senkans, U., ... & Bobrovs, V. (2020). Recent developments in cladding-pumped doped fibre amplifiers for telecommunications systems. In: *2020 22nd International Conference on Transparent Optical Networks (ICTON)* (pp. 1–6). 19–23 July 2020, Bari, Italy, IEEE.
9. Choi, I. S., Park, J., Jeong, H., Kim, J. W., Jeon, M. Y., & Seo, H. S. (2018). Fabrication of 4× 1 Signal Combiner for High-Power Lasers Using Hydrofluoric Acid. *Optics Express*, *26* (23), 30667–30677.
10. Zhu, X., Wang, K., Wang, F., Zhao, C., & Cai, Y. (2018). Coupling Efficiency of a Partially Coherent Radially Polarized Vortex Beam into a Single-Mode Fibre. *Applied Sciences*, *8* (8), 1313.
11. Guay-Lord, R., Attendu, X., Lurie, K. L., Majeau, L., Godbout, N., Bowden, A. K., ... & Boudoux, C. (2016). Combined Optical Coherence Tomography and Hyperspectral Imaging Using a Double-Clad Fibre Coupler. *Journal of Biomedical Optics*, *21* (11), 116008.

12. Dikmelik, Y., & Davidson, F. M. (2005). Fibre-Coupling Efficiency for Free-Space Optical Communication through Atmospheric Turbulence. *Applied Optics*, *44* (23), 4946–4952.
13. Eydi, N., Feghhi, S. A. H., & Jafari, H. (2021). Comprehensive Approach to Determination of Space Proton-Induced Displacement Defects in Silica Optical Fiber. *Nuclear Instruments and Methods in Physics Research Section B: Beam Interactions with Materials and Atoms*, *502*, 95–101.
14. Novoa, D., & Joly, N. Y. (2021). Specialty Photonic Crystal Fibers and Their Applications. *Crystals*, *11* (7), 739.
15. Ahmad, P., Khandaker, M. U., Rehman, F., Muhammad, N., Faruque, M. R. I., Ullah, Z., ... & Bradley, D. A. (2021). Facile Synthesis of High-Quality Nano-size 10B-Enriched Fibers of Hexagonal Boron Nitride. *Crystals*, *11* (3), 222.
16. Nathanael, A. J., & Oh, T. H. (2021). Encapsulation of Calcium Phosphates on Electrospun Nanofibers for Tissue Engineering Applications. *Crystals*, *11* (2), 199.
17. Fu, J., Chen, Y., Huang, Z., Yu, F., Wu, D., Pan, J., ... & Leng, Y. (2021). Photoionization-Induced Broadband Dispersive Wave Generated in an AR-filled Hollow-Core Photonic Crystal Fiber. *Crystals*, *11* (2), 180.
18. Itoh, T., Araki, T., Ashida, M., Iwata, T., Muro, K., & Yamada, N. (2011). Optical properties. In: *Springer Handbook of Metrology and Testing* (pp. 587–663). Springer, Berlin, Heidelberg.
19. Shukla, P., & Kaur, K. P. (2013). Performance Analysis of EDFA for Different Pumping Configurations at High Data Rate. *International Journal of Engineering and Advanced Technology (IJEAT)*, *2* (5), 487–490.
20. Standard, F. (1996). 1037C: *Telecommunications: Glossary of Telecommunication Terms*. National Communication System. Technology and Standards Division. Washington, DC: General Services Administration. Information Technology Service.
21. Chen, X., Xiao, Q. R., Jin, G. Y., Yan, P., & Gong, M. L. (2015). High Coupling Efficiency and Low Signal Light Loss (2+ 1)× 1 Coupler. *Chinese Physics B*, *24* (6), 064208.
22. Xiao, Q. R., Yan, P., Yin, S., Hao, J., & Gong, M. (2010). 100 W Ytterbium-Doped Monolithic Fibre Laser with Fused Angle-Polished Side-Pumping Configuration. *Laser Physics Letters*, *8* (2), 125.
23. Zhu, X., Schülzgen, A., Li, H., Li, L., Wang, Q., Suzuki, S., … & Peyghambarian, N. (2008). Single-Transverse-Mode Output from a Fibre Laser Based on Multimode Interference. *Optics Letters*, *33* (9), 908–910.
24. Pachon, E. G., Franco, M. A., & Cordeiro, C. M. (2012). Spectral bandwidth analysis of high sensitivity refractive index sensor based on multimode interference fiber device. In: *OFS2012 22nd International Conference on Optical Fiber Sensors* (vol. 8421, p. 84217Q). International Society for Optics and Photonics.
25. Miyazaki, K., Honda, M., Kudo, T., & Kawamura, T. (1975). Theoretical and experimental considerati ons of optical fibre connector. In: *Optical Fibre Transmission* (p. WA4). Optical Society of America.
26. Tsuchiya, H., Nakagome, H., Shimizu, N., & Ohara, S. (1977). Double Eccentric Connectors for Optical Fibres. *Applied Optics*, 16 (5), 1323–1331.
27. Knox, R. M., & Toulios, P. P. (1970). Integrated circuits for the millimeter through optical frequency range. In *Proc. Symp. Submillimeter Waves* (vol. 20, pp. 497–515). Brooklyn, NY.
28. Burns, W. K., & Milton, A. (1975) Mode Conversion in Planar-Dielectric Separating Waveguides. *IEEE Journal of Quantum Electronics, 11* (1), 32–39.
29. Okamoto, K. (1990). Theoretical Investigation of Light Coupling Phenomena in Wavelength-Flattened Couplers. *Journal of Lightwave Technology*, *8* (5), 678–683.

30. Shibayama, J., Yamauchi, J., & Nakano, H. (2003). Application of the finite-difference beam-propagation method to optical waveguide analysis. In: *17th International Conference on Applied Electromagnetics and Communications* (pp. 262–265). 1–3 October 2003, Dubrovnik, Croatia, IEEE.
31. Optiwave. (n.d.). *Optiwave Photonic Software*. Available at https:// www. optiwave. com/
32. Pepper, D. W., & Heinrich, J. C. (2017). *The Finite Element Method: Basic Concepts and Applications with MATLAB, MAPLE, and COMSOL*. CRC press.
33. Deibel, J. A., Wang, K., Escarra, M. D., & Mittleman, D. M. (2006). Enhanced Coupling of Terahertz Radiation to Cylindrical Wire Waveguides. *Optics Express,* 14 (1), 279–290.
34. Wen, J., Romanov, S., & Peschel, U. (2009). Excitation of Plasmonic Gap Waveguides by Nanoantennas. *Optics Express*, *17* (8), 5925–5932.
35. Xu, P., Zheng, J., Doylend, J. K., & Majumdar, A. (2019). Low-Loss and Broadband Nonvolatile Phase-Change Directional Coupler Switches. *Acs Photonics*, *6* (2), 553–557.
36. Pidishety, S., Srinivasan, B., & Brambilla, G. (2016). All-Fiber Fused Coupler for Stable Generation of Radially and Azimuthally Polarized Beams. *IEEE Photonics Technology Letters*, *29* (1), 31–34.
37. Chamanzar, M., Scopelliti, M. G., Bloch, J., Do, N., Huh, M., Seo, D., ... & Maharbiz, M. M. (2019). Ultrasonic Sculpting of Virtual Optical Waveguides in Tissue. *Nature Communications*, *10* (1), 1–10.
38. Zhang, Y., Zhu, W., Fan, P., He, Y., Zhuo, L., Che, Z., ... & Chen, Z. (2020). A Broadband and Low-Power Light-Control-Light Effect in a Fiber-Optic Nano-Optomechanical System. *Nanoscale*, *12* (17), 9800–9809.
39. Comsol. (n.d.). *Mach–Zehnder Modulator*. Available at thttps://www.comsol.com/model/mach-8211-zehnder-modulator-5061
40. Ou, P., Yan, P., Gong, M., & Wei, W. (2004). Coupling Efficiency of Angle-Polished Method for Side-Pumping Technology. *Optical Engineering*, *43* (4), 816–821.
41. Xiao, Q., Chen, X., Ren, H., Yan, P., & Gong, M. (2013). Fibre Coupler for Mode Selection and High-Efficiency Pump Coupling. *Optics Letters*, *38* (7), 1170–1172.
42. Fanlong, D., Xinhai, Z., & Feng, S. (2018). Side Coupler Applied in a Multi-Pumped Yb-Doped Triple-Clad Fibre Laser. *Laser Physics*, *28* (12), 125106.
43. Ou, P., Yan, P., Gong, M., Wei, W., & Yuan, Y. (2004). Studies of Pump Light Leakage out of Couplers for Multi-Coupler Side-Pumped Yb-doped Double-Clad Fibre Lasers. *Optics Communications*, *239* (4–6), 421–428.
44. Mohammed, W. S., Mehta, A., & Johnson, E. G. (2004). Wavelength Tunable Fibre Lens Based on Multimode Interference. *Journal of Lightwave Technology*, *22* (2), 469.
45. Guzmán-Sepúlveda, J. R., Guzmán-Cabrera, R., & Castillo-Guzmán, A. A. (2021). Optical Sensing Using Fiber-Optic Multimode Interference Devices: A Review of Nonconventional Sensing Schemes. *Sensors*, *21* (5), 1862.

sciendo

LATVIAN JOURNAL OF PHYSICS
AND TECHNICAL SCIENCES
2022, N 5

DOI: 10.2478/lpts-2022-0037

SPHERE AND RANDOM FLAT SURFACE CONTACT

A. Leitans*, O. Linins

Institute of Mechanics and Mechanical Engineering,
Riga Technical University, 6B Kipsalas Str., Riga, LV-1048, LATVIA
*e-mail: armands.leitans@rtu.lv

The research is devoted to the elaboration of the wear part contact estimation using 3D surface texture parameters defined in the standard ISO 25178-2:2012 for contact (it is known that elastic contact gives less wear rate) area, friction, and wear rate determination. In our research, the sphere and random flat surface model was used, where the height of surface asperities h(x, y) had a normal probability distribution. As a result of research, the equations for estimation of the elastic contact area were derived and, we obtained conditions at which it was possible to use equations for flat random surfaces. The results of this study could have wide practical application, for example, in design, choosing the geometrical and physical-mechanical parameters of the parts, calculation of real stresses, wear rate and life time of contact parts, etc.

Keywords: *3D texture parameters, contact area, elastic contact, flat surface.*

1. INTRODUCTION

The paper presents a calculation of the contact between a smooth sphere and a flat rough surface, where the case when two-plane contact theory can be used under certain conditions is considered. Contact parts can be defined as a sphere that is considered to be absolutely rigid, and its surface is smooth (arithmetic mean of the absolute height Sa <0.01 μm) and the contact pair has a flat rough surface with a defined Sa value; a flat surface can be defined as isotropic, elastic surface.

This type of contact is used in measuring instruments, sinus mechanisms, pin-on-disc type tribometer, etc. Similar calculations of sphere and plane contact are also considered in several works [1]–[7], where surface contact is defined as elastic, plastic, and elastic-plastic [8]. Finite element modelling methodology and fractal surface modelling are often used for contact modelling and calculations [9]. Sometimes, the surface contact area calculation does not take into account the texture parameters, which affects the accuracy of the contact area determination.

2. ANALYTICAL CALCULATION

The contact problem of an elastic sphere with the plane is solved in the classical theory of elasticity without considering the roughness of real bodies in mechanical engineering. The contact problem solving, taking into account the roughness, was examined in the research [4]. However, the numerical methods proposed in [4] do not give the analytical expressions for calculation of the real contact area, etc.

This study is devoted to the elaboration of a new methodology for the wear part contact estimation using 3D texture parameters.

The surface machined by abrasive instruments (grinding, polishing, honing, wearing, etc.) has an irregular surface texture, which can be described by a random function. The irregular surface is expressed by random field *h(x,y)* of two variables *x* and *y*, which are Cartesian coordinates of the surface point, where the height of surface asperity *h(x,y)* has a normal probability distribution.

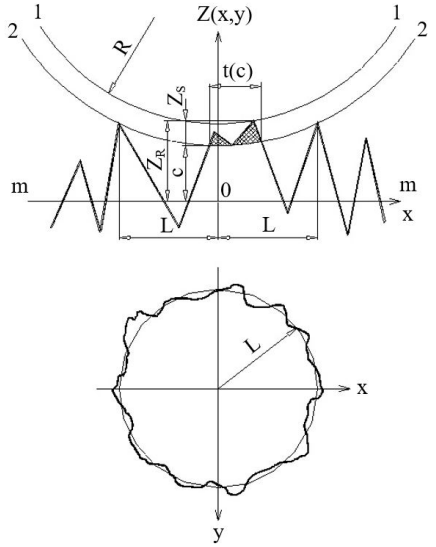

Fig. 1. Smooth sphere and rough flat surface contact.

The contact given in Fig. 1, the length of which is 2L, is formed by a rough flat surface Z_r *(x; y)* and a sphere Z_s *(x, y)*. The rough flat surface Z_r *(x, y)* is a random function described by a two-dimensional normal random field with parameter *Sq*. In turn, Z_s *(x, y)* is a deterministic function that determines the surface area of a sphere segment. *R* is a radius of the sphere, here it is assumed that the sphere is non-deformable or absolutely hard and perfectly smooth; *h (x; y)* – the height of flat surface roughness with coordinates *x, y*; *m-m* – the level of the middle plane of the rough surface; *L* – a radius of the contact area; *t(c)* – a smooth sphere and rough plane contact support line; $S_{sp.i}$ – a real contact area of the *i*-th roughness asperity at the level *c*,

Contact between these two surfaces is formed, if

$$Z_r(x,y) > Z_s(x,y) + c, \quad (1)$$

where *c* – a deformation level, subtracted from the mean plane of the rough surface *(m-m)*.

To determine the contact area of these surfaces, we will first analyse the surface cross-sectional area, the area formed by the surfaces overlapping each other without deformation. The section of such area along the x-axis is denoted in Fig. 1 by *t(c)*.

If the contact of these surfaces is homogeneous, i.e., in all sections through the vertical axis *z* it is identical, and their slice analysis can replace the contact analysis for the two surfaces:

$$Z_r(x) > Z_s(x) + c\ . \quad (2)$$

The distribution density of the random function Z_r in the case of a normal field is:

$$f(z_r) = \frac{1}{\sigma\sqrt{2\pi}} e^{-\frac{z_r^2}{2\sigma^2}} , \quad (3)$$

which is an average value, the expression of the determined function Z_s against the level c can be found using simple geometric relations (see Fig. 2).

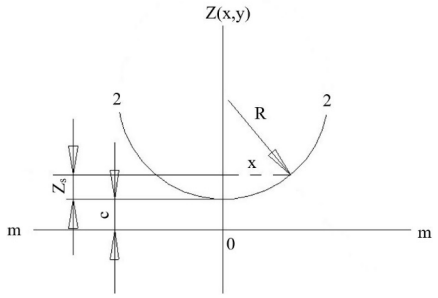

Fig. 2. Sphere segment calculation.

According to the Pythagorean theorem,

$$x^2 + (R - Z_s)^2 = R^2 . \quad (4)$$

From this equation,

$$Z_s = R - \sqrt{R^2 - x^2} . \quad (5)$$

Using inequality (2),

$$Z_r - (R - \sqrt{R^2 - x^2}) > c ,$$

the length of the slice t(c) in the contact zone *2L* can be determined as the difference between the components of the random variable and the constant function:

$$t(c) = 2\int_0^L \xi(Z_r, c)dx - \frac{2}{2L}\int_0^L (R - \sqrt{R^2 - x^2})dx = I_1 - I_2. \quad (6)$$

The first integral I_1 determines the well-known roughness support length:

$$I_1 = 2\int_0^L \xi\,(Z_r, c)dx , \quad (7)$$

where $\xi\,(Z_r, c)$ is a random variable with only two values:

$$I_1 = 2\int_0^L \xi\,(Z_r, c)dx ,$$

then

$$I_1 = 2\int_0^L E\,\{\xi(Z_r, c)\}dx = 2\int_0^L P\,\{Z_r > c\} = 2\int_0^L \int_c^\infty f(Z_r)dZ_r dx = 2L\left[1 - \Phi(\frac{c}{Sq})\right], \quad (8)$$

where
E {…} – a symbol of mathematical expected value;
P {…} – a probability symbol.

The second integral I_2 represents a constant function. It is normalized to the sphere radius *R*:

$$I_2 = \frac{2}{R}\int_0^L (R - \sqrt{R^2 - x^2})\,dx = \frac{2}{R}\int_0^L R\,dx - \frac{2}{R}\int_0^L \sqrt{R^2 - x^2}\,dx = \frac{2RL}{R} - \frac{2R}{R}\cdot\int_0^L \sqrt{1 - \left(\frac{x}{R}\right)^2}\,dx. \quad (9)$$

The second part of integral I_2 is not expressed in elementary functions. Therefore, we calculate it approximately as the area of a rectangle because the subintegral

function at the used *R, L* values is close to the rectangle:

$$\frac{2R}{R}\int_0^L \sqrt{1-\left(\frac{x}{R}\right)^2}\,dx \approx \frac{2R}{R}L\sqrt{1-\left(\frac{L}{R}\right)^2}. \quad (10)$$

Inserting formulas (8), (9), (10) in expression (6), we obtain

$$t(c)=2L\left[1-\phi\left(\frac{c}{Sq}\right)\right]-2L\left[1-\sqrt{1-\left(\frac{L}{R}\right)^2}\right]. \quad (11)$$

Introducing the concept of relative support length, which is well known in the theory of surface contact [10],

$$\eta_{sec}(\gamma)=\frac{t(c)}{2L}=[1-\phi(\gamma)]-\left[1-\sqrt{1-\left(\frac{L}{R}\right)^2}\right], \quad (12)$$

where $\gamma=\frac{c}{Sq}$ – a relative section level;
$\eta_{sec}(\gamma)$ – relative support length (for section).

The resulting formula (12) consists of two parts. The first corresponds to the contact of two planes, but the second part shows the effect of the sphere on the contact. A specific area value can be determined at specific *L, R,* and γ values. The value of contact length *L* is not defined in formula (12). Its value in the first approximation can be determined using the maximum value of the roughness profile ξ_{max} [10]:

$$E\{\xi_{max}\}=\sqrt{2ln\frac{L\cdot n(0)}{2}}, \quad (13)$$

where $\xi_{max} = S_t / S_q$; S_t – maximum roughness height; n (0) – a number of profile zeros per unit of track length.

If E $\{\xi_{max}\}$ = 3 and the sphere intersects the roughness at this point, we obtain from (13)

$$L=\frac{2\cdot e^{\xi max/2}}{n(0)}. \quad (14)$$

3. EXPERIMENTAL CALCULATION

Smooth sphere and rough flat surface contact. We understand a smooth surface as an absolutely hard and ideal smooth surface, although in practice, an ideal surface is rare, such an assumption nevertheless makes it easier in many cases to solve the contact problems of rough surfaces.

Figure 1 shows the two states of the contacting sphere, the initial state of the 1-1 sphere and the 2-2 state occupied by the sphere after the roughness deformation. According to the given contact model, it is necessary to perform calculations of the actual contact area or roughness deformation. Such attempts have been made in [4]–[9], but complex equations have been obtained. Let us look at the possibility of simplifying this scheme. First, we consider the overlap of geometric surfaces of contact parts, which is analysed with the help of computer simulation. The idea of this simulation is shown in Figs. 2 and 3. It should be noted that Figs. 2 and 3 give a schematic representation of the rough surface for clarity, but the real contact simulation includes the actual nature of the roughness with the correct roughness step parameters.

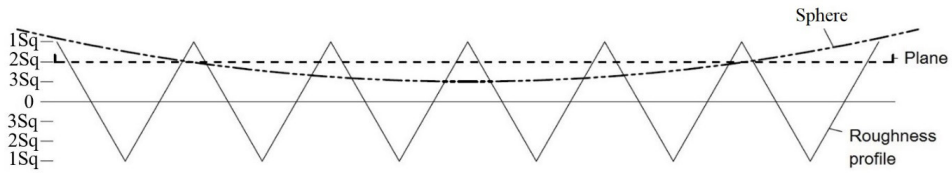

Fig. 3. Smooth sphere and smooth plane contact with a rough plane

.

Figure 3 shows the overlap of a smooth sphere and a smooth plane with a rough plane. The left side of the figure shows the contact levels in *Sq* units (*Sq* – the mean square value of the rough plane).

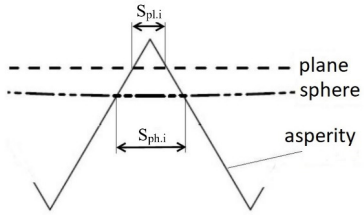

Fig. 4. Smooth sphere and smooth plane contact with one asperity.

In turn, Fig. 4 shows the contact of a smooth sphere and a smooth plane with one surface roughness ridge. The contact of the sphere with the cam occurs along the area $S_{sp.i.}$, and the plane contacts the cam with the area $S_{pl.i.}$ .The task of the given model is to position the plane so that both contact areas S_{pl} and S_{sp} are close, where S_{sp}, S_{pl} is the sum of the plane contact intersections over the entire contact area. Using computer simulation of contact (using a drawing software), it was found that when the vertex of the sphere reached the rough plane, the level of surface roughness *1 Sq* would be deducted from the centerline.

The plane should be at the level of *2Sq* (see Fig. 3). After the computer simulation, the values of smooth planes and smooth spheres for the contact cuts were found. At the roughness *Sa* parameters of 0.128–0.183 μm, 0.563–0.623 μm and 0.678–0.695 μm, the contact area of the sphere and the rough plane differed from the smooth plane contact by no more than 10 %.

The illustrated scheme of part overlap with the computer simulation method shows that under certain conditions, the sphere-plane contact can be replaced by a two-plane contact calculation methodology.

4. CONCLUSIONS

The relative support area of an ideal sphere, the rough plane, is smaller than the support area of the ideal plane, the rough plane. Although the support length formula (12) is obtained with several assumptions, in principle, it gives a correct result if, in this formula $R \rightarrow \infty$, which corresponds to the contact of two planes. Formula (12) gives: $\eta_{sec}(\gamma) = 1-\phi(\gamma)$. The latter relation describes the relative support area of two planar surfaces [10]. At the same time, this relationship confirms the results of computer simulation obtained in the research: under certain conditions, the contact of the sphere plane can be determined by the relationship of the contact of two planes.

ACKNOWLEDGEMENTS

The research has been funded by the Latvian Council of Science, project No. 2019/1-0385 "Carbon-rich self-healing multifunctional nanostructured smart coatings (NSC) for high-tech applications using high-power confined plasma technology for their deposition."

REFERENCES

1. Leitans, A., Linins, O., & Boiko, I. (2017). Contact Estimation Using 3D Surface Roughness Parameters. *Key Engineering Materials, 721*, 373–377. doi:10.4028/www.scientific.net/KEM.721.373
2. Bahrami, M., Yovanovich, M. M., & Culham, J.R. (2005). A Compact Model for Spherical Rough Contacts. *Journal of Tribology, 127*, 1147–1156. doi.org/10.1115/TRIB2004-64015
3. Greenwood, J. A., & Tripp, J.H. (1967). The Elastic Contact of Rough Spheres. *Journal of Applied Mechanics, 34* (1), 153–159.
4. Ilsums, M., & Rudzitis, J. (1971). *On a Method of Calculating the Actual Contact Area at the Contact of the Ball with the Plane in the Case of Predominantly Plastic Deformation Microroughnesses* (vol. 6). Riga, RPI: Priborostroenie (in Russian).
5. Wang, L., & Xiang, Y. (2013). Elastic-Plastic Contact Analysis of a Deformable Sphere and a Rigid Flat with Friction Effect. *Advanced Materials Research, 644*, 151–156. doi:10.4028/www.scientific.net/AMR.644.151
6. Li, L., Etsion, I., & Talke, F.E. (2010). Elastic–Plastic Spherical Contact Modeling Including Roughness Effects. *Tribology Letters, 40,* 357–363.
7. Kartini, Saputra, E., Ismail, R., Jamari, J., & Bayuseno, A. P. (2016). Analysis of the Contact Area of Smooth and Rough Surfaces in Contact with Sphere Indenter Using Finite Element Method. *MATEC Web of Conferences, 58*, 04007.
8. Mitra, A., Sahoo, P., & Saha, K. (2011). A Multi Asperity Model of Contact between a Smooth Sphere and a Rough Flat Surface in Presence of Adhesion. *Tribology in Industry, 33* (1), 3– 10.
9. Jeon, J.S., Hyun, S., & Kim, Y.S. (2007). Micromechanics on Spherical Contact with Roughness. *Key Engineering Materials, 339,* 141–146 doi:10.4028/www.scientific.net/KEM.339.141
10. Rudzitis, J. (2007). *Surface Contact Mechanics.* Part 1. Riga: Riga Technical University. (in Russian).

sciendo

LATVIAN JOURNAL OF PHYSICS
AND TECHNICAL SCIENCES
2022, N 5

DOI: 10.2478/lpts-2022-0038

OXYGEN MASS TRANSFER COEFFICIENT APPLICATION IN CHARACTERISATION OF BIOREACTORS AND FERMENTATION PROCESSES

J. Vanags*, A. Suleiko

JSC Biotehniskais centrs
27 Dzerbenes Str., Riga, LV-1006, LATVIA
*e-mail: btc@edi.lv

This review article covers the topics of evaluation and experimental determination of oxygen mass transfer coefficients (k_La) for their application in characterising bioreactors and fermentations processes. The article provides a comparison of different experimental approaches for determining k_La in bioreactors. Additionally, the influence of bioreactor design and fermentation parameters on k_La is discussed. The aim of the article is to provide useful information regarding the approaches for selecting bioreactors and their working regimes to achieve optimal fermentation results.

Keywords: Aeration, bioreactor, biotechnology, fermentations, k_La, mixing.

1. INTRODUCTION

In aerobic microorganism cultivation processes, it is necessary to supply nutrients and oxygen to the microorganism cells. The oxygen supply to the cells is more problematic because usually oxygen solubility is significantly lower compared to glucose and other components of the nutrient media. Oxygen is supplied to the cells by air bubbles, which are introduced into the bioreactor through a sparger or through the headspace. These bubbles are dispersed by mixing. The latter is necessary to supply the oxygen to the cells with sufficient intensity. Insufficient oxygen supply is often the reason for not reaching the required biomass concentrations. To ensure sufficient intensity of oxygen supply, the bioreactor must be properly designed and the appropriate mixing and aeration modes must be provided. The k_La parameter is used to characterise the oxygen mass transfer.

2. GENERAL PRINCIPLE OF k_La

Basically, the volumetric oxygen mass transfer coefficient k_La is the parameter that controls the rate of how oxygen makes a transition from the gas phase to the liquid phase. k_La shows numerically how efficiently oxygen, which is introduced through a sparger in the vessel, is dissipated and distributed in the medium by the mixer.

The notion of k_La arises from the two-film theory, which postulates that the mass transfer between two phases takes place through a boundary layer, between those two phases (see Fig. 1).

The rate of diffusion of a component between phases is dependent on the mass transfer coefficient, for liquids this coefficient often is written as k_L. The overall rate of mass transfer between two phases apart from k_L is also dependent on the contact area between those two phases, often termed a. When we combine the two, we get our volumetric oxygen mass transfer coefficient k_La.

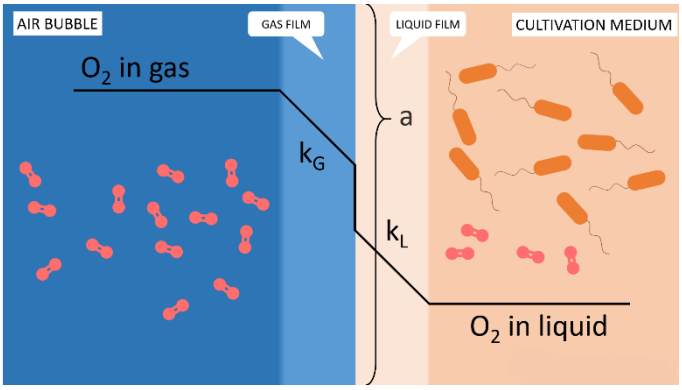

Fig. 1. Gas–liquid oxygen mass transfer according to the two-film theory.

Another important aspect of k_La can be described using the following equation:

$$dC/dt = k_La \cdot (C^*\text{-}C_L) = OTR - OUR, \quad (1)$$

where
C^* – the saturated dissolved oxygen concentration;
C_L – the current concentration of dissolved oxygen in the media.

This equation shows that the rate of oxygen concentration change in the liquid medium is dependent on k_La and the difference between the current (C_L) and maximal possible (or sometimes termed equilibrium C^*) oxygen concentrations. Simultaneously, the rate of the oxygen concentration change is equal to the difference between the oxygen transfer rate to the cultivation medium (OTR) and the oxygen uptake rate (OUR). If the OTR is higher than the OUR term, the medium will inevitably get saturated by oxygen until reaching the equilibrium concentration. On the other hand, if we observe a completely different situation, where the OUR term is larger than OTR, the oxygen concentration will fall below a required level, which would be unsuitable for supporting microorganism growth. Both situations are unfavourable due to the fact that

most often a specific organism requires a certain concentration of oxygen to be maintained; too high oxygen concentrations can lead to a completely different fermentation paths, while too low oxygen concentrations can lead to biomass growth and/or target product secretion inhibition.

As a result, one of the most widely used means of controlling the dissolved oxygen concentration is the regulation of the mixing intensity during fermentations (dissolved oxygen concentration can also be controlled by airflow, oxygen enrichment, overpressure, substrate feeding).

3. EVALUATION POSSIBILITIES OF k_La

The evaluation of k_La is important for the selection of a bioreactor for a particular cultivation process. The latter is critical for pilot and industrial scale applications because at a laboratory scale bioreactors usually easier achieve the necessary oxygen transfer rates. Often, based on the cultivation results in a laboratory scale system, pilot and/or industrial scale bioreactors are selected. It is more convenient to start k_La evaluations by using theoretical calculation equations. However, the following factors can limit the applicability of theoretical k_La calculations:

1. The chemical composition of the applied medium differs in principle;
2. The applicability of a particular k_La empirical equation depends on the limits of the parameters at which it was developed.

The applicability of experimental k_La determination methods is narrowed in the following cases:

1. The existing k_La formulas are not applicable to the selected bioreactors design;
2. The necessity to evaluate k_La in real fermentation processes.

Theoretical Evaluation of k_La

One of the most referred methods of correlating k_La with different bioreactor working modes is the empirical correlation proposed by Van't Riet in 1979 [1]. He proposed to correlate the volumetric oxygen mass transfer coefficient in a stirred-tank bioreactor with the specific power input and superficial gas velocity.

$$k_La = C \cdot (P_g/V)^{\alpha} \cdot v_g^{\beta}, \quad (2)$$

where
P_g – aerated power input, W/m^3;
V – working volume, m^3;
v_g – superficial gas velocity, m/s.

$$v_g = Q \cdot S^{-1}, \quad (3)$$

where
Q – an air flow rate, m^3/s;
S – a cross-section area in diameter plane, $S = \pi \cdot D^2 \cdot 0.25$, where D – diameter of the vessel.
C, α, β – empirical constants, which incorporate the geometry of the vessel (mixer rotors, baffles, other parts), and according to Van't Riet the mentioned coefficients are estimated as follows: C=0.026, α=0.4 and β=0.5 [1].

This formula was developed based on data for pure water, the volume of applied reactors reaches 2600 litres and specific power inputs can be in the range of 500–10 000 W/m^3.

Although the correlation proposed by Van't Riet was quite adequate in predicting k_La over a broad range of specific power input values, scientists soon began to realize that another term should be added to this equation. The remaining term was viscosity μ, so the modern modification of the original Van't Riets equation looks like this [2]:

$$k_La = C \cdot (P_g/V)^{\alpha} \cdot v_g^{\beta} \cdot \mu^{\delta}, \quad (4)$$

where
μ – dynamic viscosity, Pa·s.

To determine P_g, first, it is necessary to calculate the power input by the mixer P in ungassed conditions (without introducing gasses into the media):

$$P = K_N \cdot N \cdot \rho \cdot n^3 \cdot d^5, \quad (5)$$

where
K_N – power number (Newton`s number) of the mixer;
ρ – density of liquid media, kg/m^3;
d – diameter of mixer rotor, m;
N – coefficient that depends on the number and mutual location of mixer rotors.

There are limited data and correlations, which can be used for precise calculation of N. In principle, if the distance between mixers L is more than $2d$, then N can be assumed equal to the number of rotors installed on the mixer because in this case the interaction between rotors is negligible [3].

$$L > 2 \cdot d, \quad (6)$$

where
L – distance between mixers, m.

If this distance is less, then N will decrease depending on the interaction between mixer rotors.

There are different equations, which describe the relation of P_g/P. To select the most appropriate one for a particular case, it is necessary to study the parameters of the applied system and the defined ranges, for which a particular empirical correlation is applicable. The following equation was derived based on the experimental data from 0.4 –7 m diameter vessels equipped with ≤ 3 stage standard Rushton turbines [4]:

$$P_g = P/\sqrt{(1+A \cdot v_g/\sqrt{(g \cdot d)})}, \quad (7)$$

where
the constant A depends on the number of mixers:
1 mixer: A = 750;
2 mixers: A = 490;
3 mixers: A = 375.

4. THE EXAMPLE OF k_La CALCULATION

The task is to evaluate k_La in a bioreactor with the following design and operation parameters: working volume – 2000 litres; bioreactor diameter (D) – 1 m; mixer rotor diameter (d) – 350 mm; number of rotors – 2; distance between rotors – 720 mm; the applied rotors are standard Rushton turbines with a power number (K_N) – 7. The bioreactor maximal operation parameters: mixer rotation speed n = 300 rpm; airflow rate Q = 1200 L/min.

First, it is necessary to convert all values into SI:

N = 300/60 = 5 rps;
Q =1200x10^{-3}/60 = 0.02 m^3/s;
V = 2000 L = 2 m^3;
D = 350 mm = 0.35 m.

Distance between both mixer rotors is $2d$, and according to Eq. (6):

$N = 2$.

The ungassed power input P can be calculated using Eq. (5):

$P = 7 \cdot 2 \cdot 10^3 \cdot 5^3 \cdot 0.35^5 = 7 \cdot 2 \cdot 10^3 \cdot 125 \cdot 5.25 \cdot 10^3 = 9187.5$ W.

The cross-sectional area S of the bioreactor is:

$S = 3.14 \cdot 1^2/4 = 0.785$ m^2.

The superficial gas velocity is:

$v_g = Q / S = 0.02 / 0.785 = 0.025$ m/s.

Now according to Eq. (7), the maximum gassed power input can be calculated as follows:

$P_g = P/\sqrt{(1+A \cdot v_g/\sqrt{(g \cdot d)}} = 9187.5/\sqrt{(1+490 \cdot 0.025/\sqrt{(9.8 \cdot 0.35)}} = 3328.8$ W.

To determine k_La, the obtained values are used in Eq. (2):

$k_La = C \cdot (P_g/V)^{\alpha} \cdot v_s^{\beta} = 0.026 \cdot (3328/2)^{0.4} \cdot 0.025^{0.5} = 0.024 \cdot 19.43 \cdot 0.158 =$ **0.074 s^{-1}.**

Experimental Determination Methods of k_La

The most popular experimental determination methods of k_La are as follows:

- The sulphite oxidation method;
- The static gassing-out method;
- The dynamic gassing-out method;
- Oxygen balance method.

The ***sulphite oxidation*** was the first applied method for k_La determination [5]. It is based on the determination of oxygen transfer rates in aerated vessels by the oxidation of a sodium sulphite solution:

$$Na_2S0_3 + 0.50_2 = Na_2S0_4.$$

The rate of reaction is such that as oxygen enters the solution it is immediately consumed in the oxidation reaction of sulphite, so that the sulphite oxidation rate is equivalent to OTR. The dissolved oxygen concentration, for all practical purposes, will be zero and k_La may then be calculated using the following equation:

$$OTR = k_La \cdot C^*. \quad (8)$$

During the experiment, chemical measurements of the sulphite solution are carried out during solution agitation at different mixer rotation speeds and air flow rates in fixed time intervals. This is usually done by titrating the solution with thiosulphate. In this way, a graphical relationship is obtained between the amount of thiosulfate and time. The graph has a trend with a linear characteristic, where the slope of the line is equal to OTR.

The method is rather simple, but it is time consuming and relatively inaccurate. This method is almost no longer used today.

One of the most widely used experimental methods for k_La evaluation is ***the static gassing-out method*** [6]. When using this method, the medium inside the vessel first is stripped from oxygen. This can be done by introducing a second soluble gas (nitrogen is most commonly used). After

the oxygen level in the medium stabilizes at zero, or somewhat close to a zero value, the supply of nitrogen is switched off. Next, air is introduced into the medium at a constant flow rate, and then the increase in dissolved oxygen concentration is monitored, which can be described by the following equation:

$$dC_L/dt = k_L a \cdot (C^* - C_L). \quad (9)$$

Integration of Eq. (9) yields:

$$\ln(C^* - C_L) = - k_L a \cdot t. \quad (10)$$

Thus, a plot of against time will yield a straight line of slope , as shown in Fig. 2.

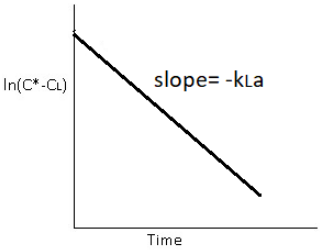

Fig. 2. Graph of $\ln(C^*-C_L)$ vs. experiment time (for determining $k_L a$).

The static gassing-out method is quite easy to perform although multiple aspects have to be taken into account in order to obtain precise $k_L a$ data: the response delay of the probe, which is used for oxygen measurements, and temperature/pressure control during the experiment.

Considering the case of the ***dynamic gassing-out method***, it is quite similar to the static method, although it has a couple of advantages [7]. Using the dynamic method, it is possible to determine the volumetric oxygen mass transfer coefficient during fermentation processes. This is done by ceasing the aeration (point A in Fig. 3) until the oxygen concentration reaches a critical point (point B in Fig.3). After that, the aeration is restored (point B in Fig.3) and DO level vs. time data is gathered.

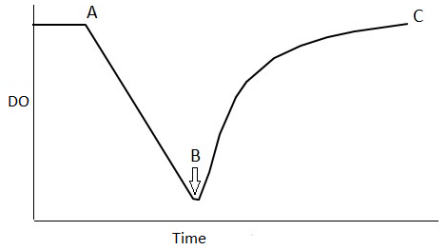

Fig. 3. Dynamic gassing-out experiment time dependent process data.

The transition of oxygen from the gas to the liquid phase is described by the following equation [2]:

$$\ln((C^* - C)/(C^* - C_o)) = - k_L a \cdot t, \quad (11)$$

where
C_o – dissolved oxygen concentration before restarting the aeration (see point B in Fig. 3);
C – dissolved oxygen concentration at time t (within the line segment BC).

Performing DO measurements and using the obtained data in Eq. (7), the following graph (see Fig. 4) is created:

$$f(t) = \ln((C^* - C)/(C^* - C_o)), \quad (12)$$

where the slope of this graph is $- k_L a$.

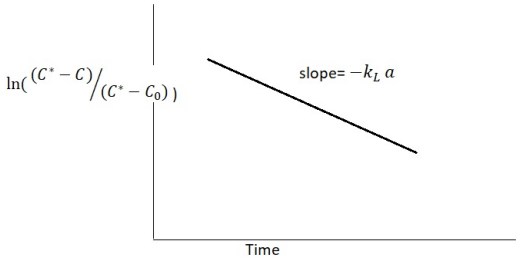

Fig. 4. Graphical function to determine $k_L a$ according to Eq. (11).

The oxygen balance method is considered more precise than the two previously mentioned approaches for $k_L a$ determina-

tion because the response delay of the DO measurement probe can be neglected [8]. The principle behind the oxygen balance method is the application of gas analysers to determine the oxygen concentration in the gas phase, thus obtaining information on the amount of oxygen that is being supplied to the fermentation medium, up-taken by the microorganisms and ejected into the exhaust line. At a steady state, when the concentration of oxygen in the medium is maintained constant, the oxygen transfer rate (OTR) is equal to the oxygen uptake rate (OUR). By constructing an oxygen mass balance for this particular state, we can determine the $k_L a$ coefficient:

$$\text{OTR} = \text{OUR}. \tag{13}$$

$$\text{OTR} = Q_{O2\text{-}IN} - Q_{O2\text{-}OUT}, \tag{14}$$

where
$Q_{O2\ IN}$ and $Q_{O2\ OUT}$ are inlet and outlet oxygen volumetric flow rates.

$$\text{OUR} = Q_{O2\text{-}V} \cdot V, \tag{15}$$

where
$Q_{O2\text{-}V}$ – a volumetric oxygen uptake rate,
V – volume of fermentation or model media.

At a steady state, the rate at which oxygen transfers from the gas phase to the liquid phase is equal to the rate of consumption of the oxygen by microorganisms:

$$k_L a \cdot (C^* - C_L) = \text{OUR}/V. \tag{16}$$

Combining Eqs. (9)–(12), the equation for determining $k_L a$ is obtained:

$$k_L a = (Q_{O2V\text{-}IN} - Q_{O2\text{-}OUT})/(V \cdot (C^* - C_L)). \tag{17}$$

Although the method gives quite precise estimates of the volumetric oxygen mass transfer coefficient, it is significantly more expensive to perform, taking into account that gas analysers are required.

5. THE INFLUENCE OF THE BIOREACTOR DESIGN ON $k_L a$

Equation (2) shows the influence of specific power input and aeration (superficial gas velocity) on $k_L a$. The mentioned equation does not encompass the effect of mixer rotor design on the mass transfer rate.

Mixer Rotor Design

The mixer rotors have to ensure both bulk mixing and dispersion of gas bubbles in the medium. For example, if two axial mixers (for example, pitched-blade impellers) are installed in the bioreactor, then bulk mixing in the whole volume will be ensured, but dispersion of gas bubbles most likely will not be optimal. If gas flow rates are high, but dispersing is not effective, then, for example, such an unfavourable effect as impeller flooding can appear which drastically decreases the OTR. To intensify gas bubble dispersion, one possible solution could be the installation of a primary rotor (in the bottom part of the vessel) with good gas dispersing properties (e.g., SCABA, Rushton etc.).

Sparger Design

The sparger design determines the bubble size and their distribution in bioreactor volume. Theoretically, if the bubble size is smaller, then $k_L a$ must be higher due to

an increase in a (contact area between the gas and liquid phases). However, smaller bubbles also pose a negative effect on oxygen mass transfer. It should be taken into account that small enough bubbles begin to express rigid body properties. The bubbles behave like a rigid sphere with less internal recirculation, so that oxygen gas molecules within the bubble do not reach the surface. If the bubble diameter is small, the bubble rise velocity will also be small. As a result, smaller bubbles contain a smaller quantity of oxygen, which would be transferred quickly. According to the literature data, the optimal size of the bubble is about 2–3 mm [9], and this must be taken into consideration when selecting the appropriate gas sparger.

6. THE CORRELATION OF $K_L A$ AND CELL GROWTH RATE DURING CULTIVATION

By determining $k_L a$ theoretically or experimentally in model media, an obviously assumption is that higher $k_L a$ will ensure higher biomass growth rates. However, in real applications different phenomena can manifest, which can negatively affect the process performance depending on applied mixing and aeration regimes. In such cases, theoretically 'better' bioreactor designs will not always guarantee higher biomass growth rates at higher predetermined $k_L a$ values.

The following phenomena can potentially drive the deviations of the predicted vs. real biomass growth rate in respect to $k_L a$:

6.1. Rheological Properties of the Fermentation Media

If the viscosity of the cultivation media and the related parameters (for example, pseudo plasticity) increases during the process, the distribution of the introduced mixing energy in the reactor volume changes. For example, in the case of relatively small viscosities, most effective mixing will be achieved using standard Rushton turbines. However, at higher viscosities, other mixer rotor designs will be more suitable. The latter can be explained by the fact that Rushton turbines generate pronounced locally intense flux zones and the agitation energy value falls lower faster near the reactor walls at higher viscosities. As a result, the decrease of OTR using standard Rushton turbines can be more pronounced in this case.

6.2. The Morphological Changes of Microorganisms by Mixing

Some types of microorganism cells are sensitive to intense mixing. This regards, for example, to mammalian and plant cells, mycelial microorganisms and algae cultures. Too intense mixing can induce changes to the cell morphology, resulting in a decrease in a growth rate. However, a decrease in the mentioned growth rate is attributed to a decrease in OUR. In such cases, mixers and their operating modes must be selected, which do not yet induce critical shear stresses to the cells. For shear sensitive cultures, standard Rushton turbines are usually not the best choice. In such cases, the use of shear sensitive mixers, such as pitched-blade impellers, propellers or similar are recommended.

6.3. Foaming

The high degree of aeration and agitation required in fermentations frequently gives rise to the undesirable phenomenon of foam formation. The presence of foam may also have an adverse effect on OTR. On the other hand, all antifoams are surfactants and are expected to have some effect on OTR. Antifoams tend to decrease OTR; it also causes a collapse of bubbles in foam but they may favour the coalescence of bubbles with the liquid phase, resulting in larger bubbles with a reduced surface area to volume ratio and hence a reduced OTR.

7. OXYGEN UPTAKE RATE

During biomass growth, the microorganism oxygen demand increases. This demand is characterised by the volumetric oxygen uptake rate OUR, which is described by the term:

$$\text{OUR} = Q_{O2} \cdot X, \tag{18}$$

where

Q_{O2} – a specific oxygen uptake rate (mmoles O_2/g biomass, h^{-1});

X – biomass concentration, g/L.

Q_{O2} depends on the microorganism strain and applied substrate. Table 1 summarises the specific oxygen uptake rates Q_{O2} for different microorganisms and substrates [10].

Table 1. Examples of the Specific Oxygen Uptake Rate for Different Microorganism Strains

Type of microbial culture	Carbon source	Q_{O2}, (mmol/g·h)
Aspergillus niger	Glucose	1.6
Beneckea natriegens	n-Propanol	12
Penicillium chrysogenum	Lactose	1.2
Saccharomyces cerevisiae	Ethanol	10
Streptomyces aureofaciens	Corn starch	7.0
Streptomyces coelicolor	Glucose	7.4
Streptomyces griseus	Meat extract	4.1
Xanthomonas campestris	Glucose	4.5

The task of the bioreactor is to ensure the supply of oxygen to the cells until no other growth limiting factors come into play. This characterises the volumetric oxygen transfer rate:

$$\text{OTR} = k_L a \cdot (C^* - C_L), \tag{19}$$

where the designations are according to Eq. (1).

This means that until OTR > OUR, the growth of microorganisms will continue. If the OTR value is higher, then higher biomass yields will be possible to achieve. By analysing Eq. (19), it can be seen that OTR will be proportional to $k_L a$ and (C^* - C_L). By applying Eq. (19), it is necessary to take into account the cell specific oxygen consumption Q_{O2} dependence on C_L. When C_L is less than C_{crit}, Q_{O2} decreases (see Fig. 5).

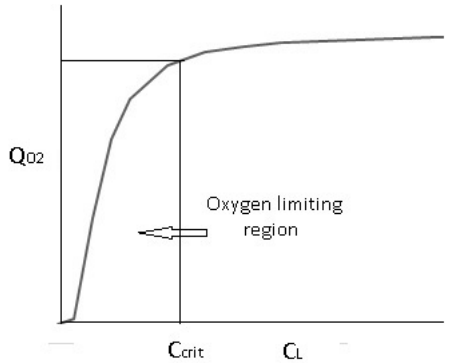

Fig. 5. Relation between the specific oxygen consumption Q_{O2} and dissolved oxygen concentration C_L.

C_{crit} can differ depending on microorganism strain and process conditions. Often C_{crit} is about 10–20 % of the equilibrium oxygen concentration C^*. C^* typically varies in the range of 6–9 mg/l.

Knowing k_La, C^* and C_{crit}, the maximum achieved biomass concentration (or in this case called critical biomass concentration X_{crit}) can be determined. If we know biomass concentration X_{max} that must be achieved in a certain cultivation process, then the necessary k_La of the bioreactor can be evaluated by maximal operating values of mixer rotation speed n and gas flow rate Q (if another limiting factor does not comes into play).

Taking into account the above-mentioned information, it can be concluded that the maximal biomass concentration will be achieved, if OTR = OUR and $C_L = C_{crit}$.

$$k_La \cdot (C^* - C_{crit}) = Q_{O2} \cdot X_{crit} \quad (20)$$

and from Eq. (20) follows that:

$$X_{crit} = k_La \cdot (C^* - C_{crit}) / Q_{O2}. \quad (21)$$

The biomass concentration calculated by Eq. (21) is a theoretical maximum and it will be achieved only if all other cultivation conditions are maintained optimal.

The Calculation Example Using Equations of OUR

A strain of *Streptomyces coelicolor* is cultivated in a 2000 liter bioreactor according to the example mentioned above using glucose as the substrate. Equilibrium oxygen concentrations C^* is 8 mg/L. C_{crit} is 20 % of C^*.

What maximal biomass concentration can be achieved in this case?

Let us assume that $X_{max} = X_{crit}$. First, all parameters are to be defined in SI units:

$k_La = 0.074\ s^{-1}$;

$C^* = 8$ mg/L; (mg/L = 10 [kg/10^6mg] / 1 [m^3/10^3 L] = $10^3/10^6 = 10^{-3}$ kg/m^3); = $8 \cdot 10^{-3}$ kg/m^3;

$C_{crit} = 0.2 \cdot 8 = 1.6 \cdot 10^{-3}$ kg/m^3.

Q_{O2} according to the table seen above for *S. coelicolor* is 7.4 mmol/g·h.

1 mol O_2 = 32 g O_2; 1mmol O_2 = $32 \cdot 10^{-3}$ g O_2 ; 1mmol O_2 = $32 \cdot 10^{-6}$ O_2 kg;

1 g=10^{-3} kg; 1h=$3.6 \cdot 10^3$ s;

Q_{O2} = 7.4 mmol/g·h = $(7.4 \cdot 32 \cdot 10^{-6}) / (10^{-3} \cdot 3.6 \cdot 10^3) = 65.8 \times 10^{-6}$ kg/kg·s;

$X_{crit} = (0.074 \cdot (8-1.6) \cdot 10^{-3}) / (65.8 \cdot 10^{-6}) = 7.2$ kg/m^3 = 7.2 g/L.

This means that the maximal biomass concentration of 7.2 g/L can be achieved during *Streptomyces coelicolor* cultivations in the defined bioreactor.

8. CONCLUSIONS

From the information presented above, the following conclusion can be drawn regarding k_La as a bioreactor efficiency parameter:

1. The theoretical calculation equations of k_La with satisfactory accuracy are applicable to popular mixer rotor types (Rushton turbine, pitched-blades, etc.) and for bioreactor volumes of up to 3000 liters.
2. Experimental methods are labour-intensive, but if the mixing system consists of different or not widely applied mixer rotors, then it is recommended to determine k_La experimentally for scale-up purposes.
3. Using experimental methods, it is possible to determine k_La during running cultivation processes (dynamic gassing-out and oxygen balance methods).
4. The determined k_La usually correlates sufficiently with the growth of biomass during the cultivation process, as long as it is not significantly affected by cultivation-related phenomena (rheology, morphology, foaming).
5. Oxygen uptake rate differs for different cultivation processes depending on the microorganism type and applied carbon source. This means that when selecting the scale-up bioreactor and its parameters for a particular process, it is desirable to know Q_{O2} of the applied microorganism strain. The latter will dictate what k_La bioreactor should be chosen to provide sufficient OTR for obtaining targeted biomass/product yields.

ACKNOWLEDGEMENTS

In accordance with contract No. 1.2.1.1/18/A/007 between VMKC Ltd. and the Central Finance and Contracting Agency, the study is conducted by Biotehniskais centrs JSC with support from the European Regional Development Fund (ERDF) within the framework of the project “Competence Centre of Smart Materials and Technologies”.

REFERENCES

1. Van’t Riet, K. (1979). Review of Measuring Methods and Results in Nonviscous Gas–Liquid Mass Transfer in Stirred Vessels. *Ind Eng Chem Process Des Dev., 18*, 357–364.
2. Garcia-Ochoa, F., & Gomez, E. (2009). Bioreactor Scale-up and Oxygen Transfer Rate in Microbial Processes: An Overview, *Biotechnol. Adv., 27*, 153–176.
3. Hudcova, V., Machon, V., & Nienow, A.W. (1989). Gas–Liquid Dispersion with Dual Rushton Turbine Impellers. *Biotech. Bioeng.,* 34, 617–628.
4. Mockel, H.O., Weissgarber, H., Drewas, E., & Rahner, H.J. (1990). Modelling of the Calculation of the Power Input for Aerated Single and Multistage Impellers with Special Respect to Scale-up. *Acta Biotechnol., 10*, 215–224.

5. Cooper, C.M., Fernstrom, G.A., & Millers, S.A. (1944). Performance of Agitated of Gas-Liquid Contactors. *Ind. Eng. Chem*., *36*, 504–509.
6. Wise, W.S. (1951). The Measurement of the Aeration of Culture Media. *J.Gen.Micro*., *5*, 167–177.
7. Taguchi, H., & Humphrey, A.E. (1966). Dynamic Measurement of the Volumetric Oxygen Transfer Coefficient in Fermentation Systems. *J. Ferm. Technol., 44* (12), 881–889.
8. Casas, L. (2006). Simultaneous Determination of Oxygen Consumption Rate and Volumetric Oxygen Transfer Coefficient in Pneumatically Agitated Bioreactors. *Industrial & Engineering Chemistry Research, 45* (3), 1167–1171.
9. Rao, D.G. (2010). *Introduction to Biochemical Engineering* (2nd ed.). India: Mc Graw Hill.
10. Pauline, M.D. (2013). *Biochemical Engineering Principles* (2nd ed.). Netherlands: Elsevier.

sciendo

LATVIAN JOURNAL OF PHYSICS
AND TECHNICAL SCIENCES
2022, N 5

DOI: 10.2478/lpts-2022-0039

INFLUENCE OF INTERNAL GAS PIPELINES BUILT INTO THE STRUCTURE ON THE SAFETY OF RESIDENTS AND ENERGY EFICIENCY FACTORS OF THE BUILDING

A. Romanovs, J. Tihana, N. Kondrahins*

Department of Heat Engineering and Technology,
Riga Technical University
6 Kipsalas Str., Riga, LV-1048, LATVIA
*e-mail: kondrahin.nikita@gmail.com

With an emphasis on the visual appearance of buildings, surface and internal gas pipelines are being built into structures and walls, which can affect system serviceability and occupant safety. When placing gas pipelines in a closed room (shafts, ducts, facade structures, etc.) there is a risk that in case of leakage, natural gas will accumulate in the room, which together with the ambient air, within the specified concentration limits, forms an explosive mixture. The present paper analyses the built-in internal gas pipeline systems, their installation norms, operation and maintenance problems in different types of buildings. It is shown that requirements do not cover all possible gas pipeline installation options. The analysis of the gas supply system operator shows that non-compliance with the applicable norms has been identified in every third of the 400,000 gas consumers in Latvia in the surface and internal gas pipeline system. To improve and develop safety requirements, it is planned to perform an experiment that is described in detail in this paper. Pre-experimental calculations are made to set reference points in the study and find the main influencing parameters on gas leakage process.

Keywords: Building, explosion hazard, gas pipeline system, installation, installation of structures, internal system, natural gas, operation, safety.

1. INTRODUCTION

Natural gas (CH_4) is a highly flammable combustible substance. If the necessary safety measures are not observed and it reaches a concentration of 5–15 %, it can cause an explosion. Nevertheless, natural gas systems have crashes around the world every year [1]. As a result of gas leaks or explosions, people suffer and die. The city of Jelgava experienced a severe tragedy 50 years ago with a natural gas leak. 41 people, including 14 children, died due to natural gas explosion in the basement of a residential building. The summary of the number of natural gas leaks prevented by the Emergency Service of the Latvian Natural gas Distributing System Operator (DSO) for 2019 is provided in Fig. 1 [2].

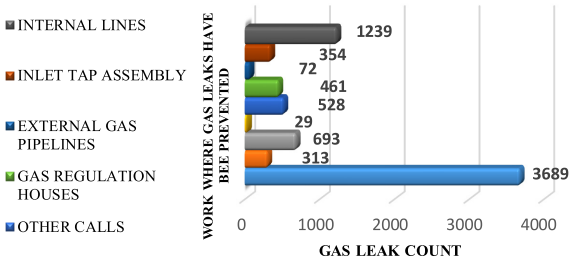

Fig. 1. The number of leaks prevented by the Emergency Service in 2019.

Figure 1 shows that a majority or 71 % of leaks occur in internal (and related) gas pipeline systems. Similar situation has been observed in previous years. Statistics shows that the internal gas pipeline system and its units are most safety risk zones. As it is described in Section 3, internal pipelines are hidden inside construction elements that create a barrier for leakage early detection. This problem can also be relevant for built-in HVAC system, for example, the use of panels with a built-in air duct in construction [3]. The authors believe that construction regulatory bodies shall consider these cases of internal gas pipeline installation. Analysing the existing studies on similar issues, e.g., [4]–[7], it was found that there were no simulations performed on natural gas leakage from pipeline installed inside construction elements. Considering the safety of construction and internal utilities, it is necessary to take into account their negative impact on energy efficiency [8]. The present study consists of the Latvian construction regulatory analysis, pipeline installation statistical analysis in Latvia, planning and performing an experiment, result analysis and recommendations. In this paper, we cover pre-experimental phases of the study. It should be noted than prolonged interruption in energy supply due to the repair work may require installation of addition temporary energy sources [9], which may cause extra costs.

2. REGULATORY ANALYSIS

Construction of natural gas supply engineering network systems in Latvia belongs to the regulated sphere, and it can be performed by (1) a construction organisation –

designers who have a construction merchant registration certificate issued by the Ministry of Economics of the Republic of Latvia (LR); (2) trained, certified and certified gas engineers – designers. There should be the information base and equipment required for the performance of design work; the activity is civilly insured. The information base includes relevant regulatory documents, building regulations, standards, calculation methodologies, manuals, catalogs, and other materials. Project solutions must be ensured by the Latvian Building Code (LBC) 006-00 "Essential Requirements for Structures", as well as the requirements of mandatory regulations, construction norms and standards. Solutions must be based on technical and economic calculations and environmental protection requirements [10], [11]. Currently, the normative document of 2015 expired; two other Cabinet of Ministers Regulations (CMR) 500 "General Construction Regulations" [12] and CMR 529 "Building Regulations of Buildings" [13] were adopted instead.

It is important that internal gas piping systems, including fittings, as well as control, safety and measuring devices, are designed to ensure their safe use throughout their service life [14], [15]. Such regulatory, technical regulations are implemented and controlled in most countries. In Latvia, renovation or repair of existing gas pipeline systems begins with a deliberate intention to do so. The supply of natural gas to the existing renovated, repaired gasified object is divided into four stages: (1) Requesting technical regulations from the DSO, object design and coordination works; (2) Realization of the object, construction works (assembly, repair, renovation), drawing up executive documentation; (3) Delivery of the object (inspection of the object, verification of compliance with the developed project and the developed executive documentation, verification of strength and tightness), acceptance into operation; (4) Natural gas pipeline system commissioning operation (gas supply to consumers). Types of gas pipeline system design and installation work are regulated by normative base standards, such as the Latvian National Standard LNC 417 [16] and LNC 419 [17], which envisage that the gas pipeline system is allowed to be built (assembled) as (1) an open type (see Fig. 2a) and (2) as a closed place (building a niche) (see Fig. 2b).

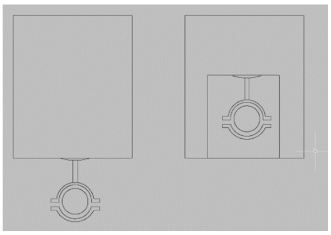

a) b)

Fig. 2. Types of gas pipeline system installation [17].

When designing and installing the internal gas pipeline system, the distances from building structures, technological equipment and other communications must be observed, which ensure convenient installation, maintenance and repair of gas pipelines and other adjacent communications. In order to prevent an explosion or the spread of fire in the event of a fire, the following measures should be taken:

- if gas pipelines are installed in ducts or shafts, their dimensions must allow for installation, operation and repair. Ducts or shafts must be in parts or fully ventilated;
- if gas pipelines are installed on monolithic floors, their built-in areas must not be subject to significant loads (vehicles, equipment, etc.) and aggressive substances. Gas pipelines, their entry and exit points shall be placed on the floor with a suitably fastened protective sleeve;

- if gas pipes are inserted in ducts in the floor, they must be covered with removable plates. The free volume of the channel can be filled with sand. The ventilation openings of the duct cover plates must ensure adequate duct ventilation.

This requirement applies to industrial objects, which now, in the authors' experience, is not used in Latvia at all, using the possibilities to install the gas pipeline in an open manner. Currently, the installation of a gas pipeline in monolithic floor constructions is being used in private single-family houses by creating a kitchen area with islands with a fireplace, as well as in public companies that provide catering services that need to create a kitchen area with an island. Each solution of this type of project is considered and agreed separately.

An emphasis on heightened security measures:

- If gas ducts are installed in a free space, such as between a suspended ceiling or between a wall and a front wall, this space must be ventilated through openings in the enclosing walls, two diagonal ventilation openings. If it is not possible to provide ventilation in the free space, the gas pipes must be fitted with protective pipes made of corrosion-resistant material or protected against corrosion, and their ends must protrude outside the free space, considering all requirements.

We believe that currently the regulatory documents responsible for gas pipeline system design LNC 417 [16] and the installation of the gas pipeline LNC 419 [17] do not pay significant attention to the above-mentioned built-in solutions. The minimum requirements required by the design standard [16] are not mentioned at all for such solutions. Standard "Gas Supply System Installation" [17] envisages the construction of only two types of internal gas pipeline systems (see Fig. 2). These types of installation are also mentioned in LBC 241-15 [15] without detailed explanation. Some aspects of ventilation and ventilation of gas pipeline installation premises are mentioned, which do not fully cover the solutions available today and do not promote safe, economically justified and efficient installation of the gas system in buildings.

The installation of the internal gas pipeline system may be performed after the following steps are finished:

- wall, ceiling, floor, bulkhead and other structures that will serve as gas pipelines and equipment support construction;
- creation of openings and channels in ceilings, walls and foundations of buildings for the installation of gas pipelines; supporting structures must be so prepared that finishing works will not affect gas pipelines and equipment;
- rooms where gas equipment will be installed on the floor must have finished floors;
- protection of gas pipelines from external factors is very important;
- for closed built-in (ducted) pipes, freely built-in steel pipes in wet (non-ventilated) rooms, corrosion protection with varnish, paint, polymer or other type of coating is required;
- polymer insulation coatings for corrosion protection of steel or copper gas pipes installed in floors;
- gas pipelines that cross building structures – ceilings, walls – must be placed in a protective shell, filled with a flexible, non-corrosive filling and sealed with a dense material that prevents moisture from entering the space between gas line and protective shell at both ends [17].

Safe gas supply is increased by installing automatic gas sensors and automatic flow interrupters. The purpose of these devices is to make a signal and interrupt the gas supply if leakage appears. The mandatory condition for the use of devices is regulated by LBN 241-15 [15]. The authors believe that if a pipeline is built-in inside closed free-space containing constructions, gas sensor implementation should be mandatory despite the fact that total gas installation cost increases.

3. REAL-LIFE CASES AND STATISTICAL ANALYSIS

After the construction of a new, renovated, reconstructed internal gas pipeline system is finished, the gas pipeline shall be inspected: its strength and tightness with air or inert gas shall be checked [10], [15]. It is one of the mandatory safety measures when commissioning an internal gas pipeline. In Latvia, the operation of the gas supply system and new object comissioning are strictly controlled by responsible services of JSC GASO that:

- participate in the strength and tightness test of the object;
- check whether the object has been built in accordance with the normative requirements and adjusted project.

The authors performed internal gas pipeline system inspection of 2506 objects in Riga and Riga district from 2011 to 2018. The results are summarised in Fig. 3 [2].

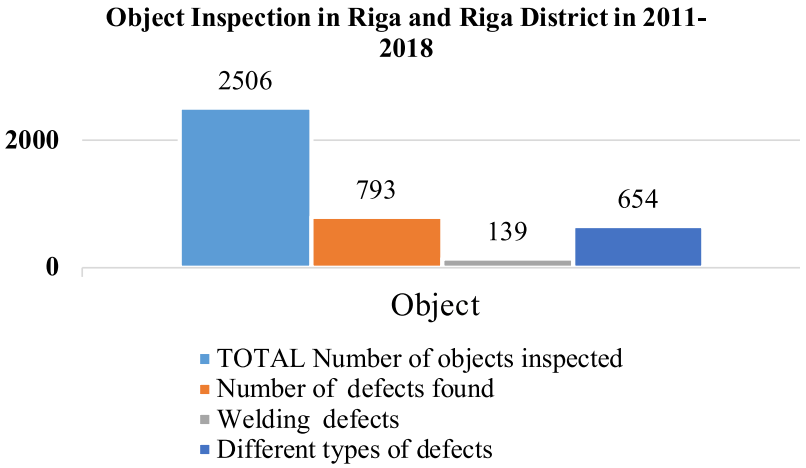

Fig. 3. Object inspections satistics in 2011–2018.

Figure 3 shows that in 793 or 31.64 % of cases the violation acts were registered, of which 139 or 17.52 % violations were related to defects of weld joints, 6 objects of the total number were not accepted at all, in 654 or 82.47 % cases other violations were found. The results of the strength and tightness test performed in all tested objects are summarised in Fig. 4 [2].

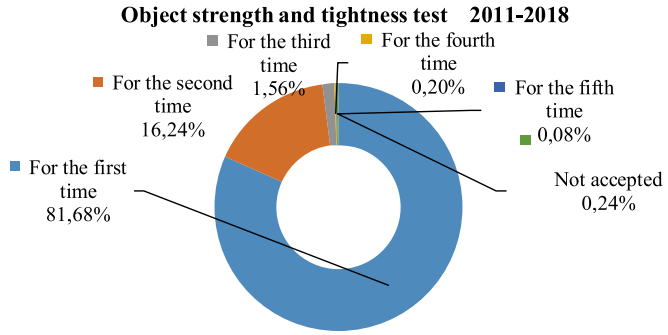

Fig. 4. Object strength and tightness test in 2011–2018.

In 81.68 % of cases, the strength and tightness test was passed from the first attempt, and 0.24% of buildings did not pass it at all. Before new, renovated, reconstructed gas pipeline was put into operation, gas leaks were detected and eliminated in an average of 20 % of cases due to "hidden defects" discovered during tests. A similar number of detected "hidden defects" was observed in the external gas pipeline system [18]. According to call statistics of the above-mentioned Emergency Service, we see that the largest part of violations was found after the acceptance of operation and operation of existing gas pipelines. One of the cases when a violation was detected was work increasing building energy efficiency. Unfortunately, very often the building insulation is not notified to the DSO, the facade insulation is underway or even completed, but later it is established that the DSO needs to exercise its right to request an initial repair. This is due to the fact that the objective need to provide access to gas pipeline inlets for maintenance or emergency repairs is regularly ignored during the renovation of the building. DSO claims are often caused by the performance of insulation work.

In the event of an emergency, the entire building will have to be shut off, repairs will follow and access to the inlet will also be required. As a result, new insulation will be damaged, the renewal of which will require additional funds. From the safety point of view, the gas outlet at the building wall is one of the most dangerous elements in a low-pressure gas pipeline system. The natural gas supply is located in an inhomogeneous environment (transition from ground to atmosphere), so the pipeline in this place is exposed to various factors, building deformations, ground fluctuations, rainwater, as well as ultraviolet radiation and temperature fluctuations.

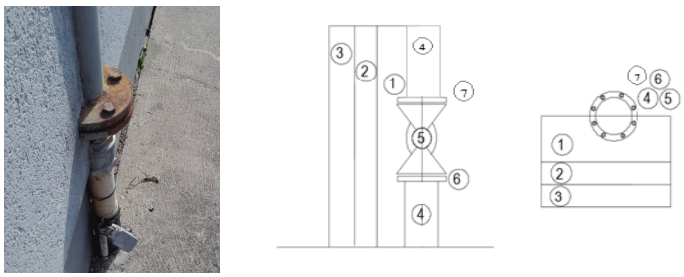

Fig. 5. Gas pipeline inlet shut-off device after building insulation works [2]: 1 – Insulation material; 2 – Air gap; 3 – Exterior foundation wall of the building; 4 – Gas pipeline; 5 – Gas line shut-off device; 6 – Gas line threaded connection with shut-off device; 7 – Gas line flange type detachable connection behind the shut-off device.

Figure 5 shows the following. During the implementation of the building energy efficiency improvement project, the existing gas pipeline DN 50 was partially built into the insulation. Before insulation works, the minimum distance between the gas pipeline and the wall of the building is 3–4 cm, which meets the requirements of LBC [15] LNC 419 [17] and LNC 445 [19], [20] standard. The distance from the outer part of the flange to the wall is 2–3 cm. After the building insulation process was completed, the gas pipeline, shut-off valves and flanges were half-installed inside isolation. This excludes the possibility to inspect, service, and also prevent gas leakage, if it occurs. In addition, during the leakage, natural gas can spread inside the insulation finishing structure, which is very dangerous. There must be no situation where customers "pay" with long-term natural gas outages and expensive repairs due to incorrect renovation of the building [21]. During the inspection period, defect acts are detected and compiled for various types of violations, in connection with non-compliance with the operating rules. According to the data of the DSO Riga section, in Riga and Riga district 21 violation acts were drawn up in 2019 and 6 of them were related to natural gas leak [2].

4. EXPERIMENT PLANNING

To create recommendations for regulatory requirements, it is planned to perform series of numeric and real-life experiments to discover possible risks in different natural gas pipeline installation solutions. The experiment is planned to be performed in two parts.

The first part of the experiment is planned to be performed with the help of the simulation program ANSYS R.18.0 Academic. It is planned to perform experiments simulating the structures of different buildings with different types of internal gas pipeline system installation (see Figs. 10–14) to study the spread of natural gas in these structures. This affects building and gas pipeline system operation, energy efficiency, and human safety.

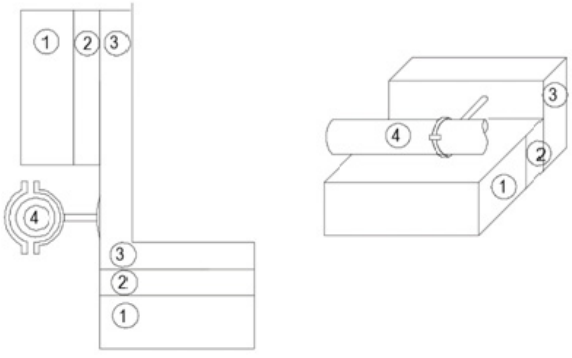

Fig. 10. Facade gas pipeline model: 1 – Insulation material; 2 – Air gap; 3 – Exterior foundation wall of the building; 4 – Gas pipeline.

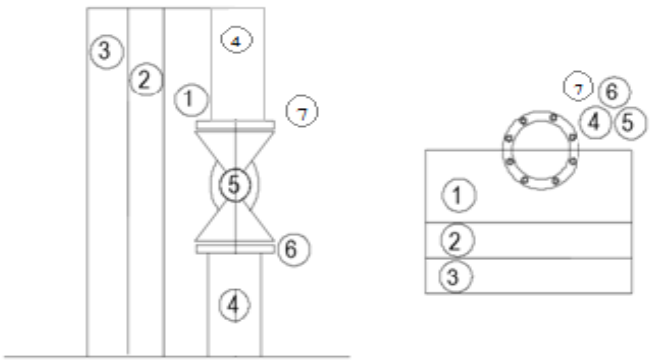

Fig. 11. Gas pipeline inlet shut-off device after building insulation works: 1 – Insulation material; 2 – Air gap; 3 – Exterior foundation wall of the building; 4 – Gas pipeline; 5 – Gas line shut-off device; 6 – Gas line threaded connection with shut-off device; 7 – Gas line flange type detachable connection behind the shut-off device.

Gas pipeline and building facades. Gas pipeline inlet shut-off device after building insulation works was described above.

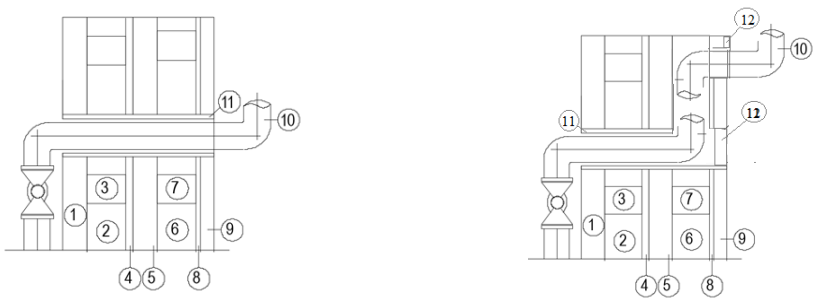

Fig. 12. Gas pipeline installation model frame type building external wall: 1 – Facade finishing boards; 2 – Air gap between the external wall of the building and the insulation material; 3 – Frame finishing boards (Lathing); 4 – Wind and steam membrane; 5– Wood fiber or USB-3 boards; 6 – Insulation material; 7 – Frame finishing boards (Lathing), 8 – Vapor barrier (film), 9 – Interior finishing material (plaster), 10 – Gas pipeline, 11 – Gas pipeline protective sleeve, 12 – Ventilation hole.

Figure 12a shows that the gas pipeline was built through the structure of the building and the interior was installed with open space. According to Fig. 12b, the pipeline is partially constructed in the load-bearing structure of the building, rising to the top and exiting the structure at the ceiling of the room. Next, the gas pipeline system is installed in the room openly. If ventilation holes (bottom and top) are formed in position 12 and ensure ventilation of the built-in frame parts of the gas pipeline, it significantly reduces the intended thickness of the insulation material at this location structure. Creating transitions from the indoor built-in vapor membrane allows indoor vapors to accumulate without restriction to accumulate thermal insulation material and uncontrollably damage the thermal insulation itself and the load-bearing wooden frame.

As the thickness of the thermal insulation decreases, dew points with condensate can form inside the frame. If the 11-position ventilation holes are not formed or intentionally closed: 1 – this is non-compliance with safety and standarts; 2 – If the insulation parameters of the building calculated at the design stage are not observed, structural defects appear. The initial reduction in the overall energy efficiency of the building in the long term can lead to structural collapse.

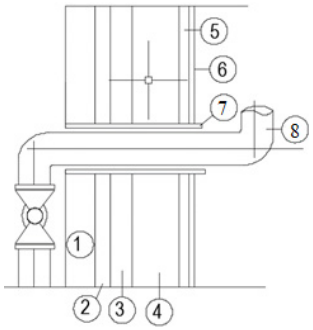

Fig. 13. Gas pipeline construction model through a frame-type building external wall SIP panel construction. 1 – Polystyrene heat layer for creating a facade part; 2 – Gas line air gap between the external wall of the building and the insulation material; 3 – USB-3 boards; 4 – Polystyrene insulation material; 5 – USB-3 boards; 6 – Interior finishing material (plaster); 7 – Gas line protection sleeve, 8 – Gas pipeline.

Examining the object of prefabricated SIP panels and their assembly technology. The advantage over classic wooden frame constructions is the directly selected SIP panel construction materials and their low thermal resistance coefficient. SIP (Structural Insulated Panel) is a structural element obtained by gluing high-density expanded polystyrene (EPS) board under pressure between two oriented OSB boards. It has been observed that in 95 % of cases the gas pipeline of SIP panel construction buildings is installed openly. In 5 % of cases, gas pipelines are installed in built partitions (false or between walls) of boiler room and kitchen. The set of buildings is designed so that the length of the indoor gas pipeline can be designed and installed as short as possible (smaller).

a) b)

Fig. 14. Gas pipeline construction model through the external wall of the building masonry (brick, aerated concrete): 1 – Facade finishing (plaster); 2 – Insulation material; 3 – Masonry wall (brick, aerated concrete); 4 – Interior finishing material; 5 – Gas pipeline; 6 – Finishing material for interior wall construction (plasterboard); 7 – Ventilation hole (bottom or pipeline height).

The use of concrete, brick, aerated concrete and other materials is also very popular in building construction in Latvia. This type of building is in principle very light and convenient when performing engineering construction work and assembly work. Communications are options to be built into building structures to hide them or install openly. Gas pipeline installation in this type of building takes place at different stages of building construction. Many of them take place during the middle stage of construction of the building when the works are in full swing. The gas pipeline is installed up to the boiler room waiting for the installation of the boiler, which can last up to a few months, until the first wave of cold snaps. In the autumn, finishing works are completed, the building is ready to receive heat. In the spring or summer pre-installed gas pipelines in half or in full are embedded in the plaster, hiding utilities behind or between the walls and ceiling. The place where the gas pipeline is located is not equipped with ventilation grilles to avoid cooling the premises and between the premises.

All the models described above will combine the problem of installing a gas pipeline in the external and internal structures of a building. When installing gas pipeline in building facades, a situation may arise that with decreasing facade insulation, the wall thickness of the inner part of the building appears and dew points appear inside the structure and in the pipeline. Long-term effects can significantly damage a building structure. The pipeline will experience increased corrosion affecting its safety. If the degree of corrosion during operation reaches critical limits, defects (cracks, pores, penetrating corrosion) appear. In the event of a damaged pipe, there will be uncontrolled gas leakage with the distribution and accumulation inside the building structure. The long-term consequences are financially disadvantageous.

In the second part of the experiment, it is planned to build an experimental model stand where some of the experimental cases performed with the help of ANSYS R.18.0 academic simulation program will be repeated.

A lot of parameters may influence gas spreading in space, for example:

- leakage outlet location, size;
- gas temperature, room temperature;
- ventilation;
- channel geometry, etc.

As the number of leakage parameter combinations with all installation options combinatorically explodes, a set of pre-experimental calculations was made taking into account some key factors to set reference points in further studies.

5. RESULTS AND DISCUSSION

In cases, when the area of the leakage hole is very small and the pressure in the gas pipeline does not exceed 100 mbar, it was decided to use a simplified calculation according to the methodology [8].

Calculation description. For pipelines with operating pressure below 90 kPa, leakage volume was calculated according to the following formula:

$$Q = \frac{3600 \cdot \mu \cdot S \cdot k_0}{\rho_0} \cdot \sqrt{8{,}45 \cdot (P + P_0) \cdot \rho \cdot \left(\left(\frac{P_0}{P + P_0}\right)^{1{,}53} - \left(\frac{P_0}{P + P_0}\right)^{1{,}76}\right)}. \quad (1)$$

For pipelines with operating pressure more than 90 kPa, leakage volume was calculated according to the formula:

$$Q = \frac{3600 \cdot \mu \cdot S \cdot k_0}{\rho_0} \cdot \sqrt{0{,}44 \cdot (P + P_0) \cdot \rho,} \quad (2)$$

where
μ – an outflow coefficient (Table 1);
S – an area of the leakage opening, m^2;
k0 – a ground flow-resistance coefficient (accepted equal to 1);
ρ0 – gas density at normal conditions, kg/m^3;
P0 – atmosferic pressure, Pa;
P – pipeline operating pressure, Pa;
ρ – pipeline gas density, kg/m^3.

Table 1. Aperture (Hole) Flow Factor Values

S/S_{int}*	< 0.1	0.1 –0.2	0.2 –0.3	0.3 –0.4	0.4–0.5	0.5 –0.6	0.6 –0.7	0.7 –0.8	0.8 –0.9	>0.9
μ	0.611	0.614	0.622	0.634	0.65	0.678	0.724	0.787	0.888	1.09

*S_{int} – a pipeline internal cross-sectional area, m^2.

$$\rho = \frac{\rho_0 \cdot (P + P_0) \cdot T_0}{P_0 \cdot T}, \quad (3)$$

where
T_0 – surrounding medium temperature, K;
T – gas temperature, K.
The following initial parameter values were accepted:

ρ_0 = 0.6882 kg/m3;
P_0 = 101325 Pa;
T_0 = 293 K;
T = 283 K;
S – 10 possible cases were considered based on the most probable defect sizes (from 0.1 to 1 mm^2).

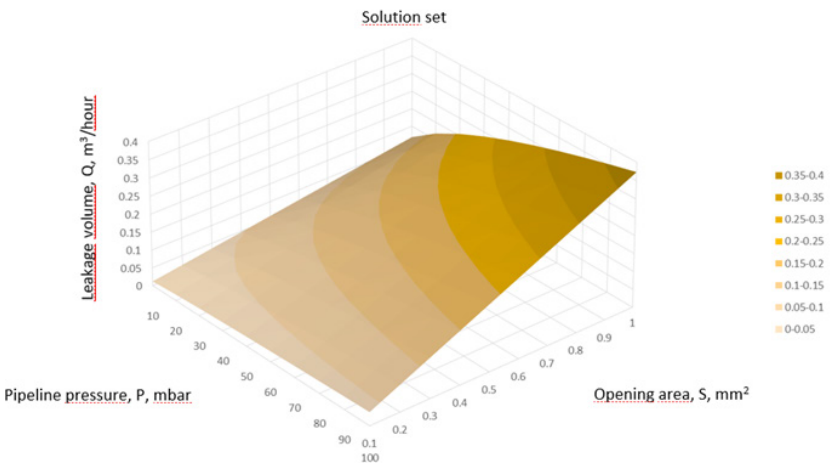

Fig. 15. The ratio of the leakage volume to the pressure in the gas pipeline and opening size.

It is seen in Fig. 15 that the higher the pressure and the larger area of leakage opening, the larger the leakage. In the considered cases, an opening area showed greater impact on leakage volume than pipeline pressure. It means that the experiment shall be performed considering different leakage opening sizes for each pipeline operating pressure category. That will increase a number of simulations, but will probably allow detecting the most dangerous leakage types for gas accumulation inside construction elements.

6. CONCLUSIONS

This paper is the first in series that will cover this study. We made a detailed analysis of the Latvian regulatory requirements in internal gas pipeline installation area, described real-life cases of pipeline installation options and showed statistics on defects. An experiment plan was given and pre-experimental calculations were performed. The course of the experiment and summart of the obtained data will be described in the next thematic articles on natural gas distribution and infiltration in building structures, ventilation in the presence of a solution in the building and its impact on reducing the distribution of natural gas in the building. Further research may be related to the appropriate type of building construction, process security measures and requirements for importing binding gas supply standards.

ACKNOWLEDGEMENT

The research has been supported by the European Regional Development Fund within the Activity 1.1.1.2 “Post-doctoral Research Aid” of the Specific Aid Objective 1.1.1 “To increase the research and innovative capacity of scientific institutions of Latvia and the ability to attract external financing, investing in human resources and infrastructure” of the Operational Programme “Growth and Employment” (No.1.1.1.2/VIAA/ /2/18/259 “Efficiency of Compact Gas Hybrid Appliance in Latvian Climate Conditions”).

REFERENCES

1. Prozuments, A., & Borodinecs, A. (2017). Indoor Air Stratification in Warm Air Supply Systems. *ASHRAE J., 59*, 54–65.
2. JSC GASO. (n.d.). *Latvian Gas Distribution System Operator Statistics*. Available at https://www.conexus.lv/latvias-gas-transmission-system
3. Borodinecs, A., Geikins, A., Barone, E., Jacnevs, V., & Prozuments, A. (2022). Solution of Bullet Proof Wooden Frame Construction Panel with a Built-In Air Duct. *Buildings, 12*. https://doi.org/10.3390/buildings12010030.
4. Merilo, E.G., Groethe, M.A., Colton, J.D., & Chiba, S. (2010). Experimental Study of Hydrogen Release Accidents in a Vehicle Garage. *Int. J. Hydrogen Energy, 36,* 2136–2444. https://doi.org/10.1016/j.ijhydene.2010.04.056.

5. Litto, R., Hayes, R.E., & Liu, B. (2006). Capturing Fugitive Methane Emissions from Natural Gas Compressor Buildings. *J. Environ. Manage., 84*, 347–361. https://doi.org/10.1016/j.jenvman.2006.06.007.
6. Hajji, Y., Bouteraa, M., Elcafsi, A., Belghith, A., Bournot, P., & Kallel, F. (2015). Natural Ventilation of Hydrogen during a Leak in a Residential Garage. *Renew. Sustain. Energy Rev., 50*, 810–818. https://doi.org/10.1016/j.rser.2015.05.060.
7. Juwari, Handogo, R., Cahyono, T., Safarudin, M., Panca Anugraha, R., Aulia, F. … & Nuur Kharisma, M. (2020). Simulation of natural gas dispersion and explosion in vented enclosure using 3D CFD FLACS software. In: I*OP Conference Series: Materials Science and Engineering* (pp. 1–12). 16–17 September 2020, Chennai, India, Institute of Physics Publishing. https://doi.org/10.1088/1757-899X/778/1/012144.
8. Prozuments, A., Borodinecs, A., Zemitis, J., & Strelets, K.I. (2020). The Effect of the Air Duct Tightness on the Stability of the Indoor Air Parameters. *Mag. Civ. Eng., 97*. https://doi.org/10.18720/MCE.97.10.
9. Zajecs, D., Lebedeva, K., & Odineca, T. (2022). Application Possibilities of the Off-Grid Hvac System Operation Solution for Temporary Shelters in the Latvian Climate Conditions. *Latv. J. Phys. Tech. Sci,. 59*, 55–63.
10. Platais, I. (2008). *Gas Supply*. Part 2. pp. 1–219. Riga: RTU Publishing House (in Latvian).
11. Ionin, A. (1989). *Gas Supply*. M.: Moscow Building Press.
12. Cabinet of Ministers. (2014). *General Construction Regulations*. Latvijas Vestnesis. Available at https://likumi.lv/ta/en/en/id/269069
13. Cabinet of Ministers. (2014). *Building Regulations*. Latvijas Vestnesis. Available at https://likumi.lv/ta/id/269164-eku-buvnoteikumi
14. Cabinet of Ministers. (2015). *Regulations Regarding the Latvian Building Code LBN 242-15 "Natural Gas External Gas Pipeline System"*. Latvijas Vestnesis. Available at https://likumi.lv/ta/id/275017-noteikumi-par-latvijas-buvnormativu-lbn-242-15-dabasgazes-arejo-gazesvadu-sistema
15. Cabinet of Ministers. (2015). *Regulations Regarding Latvian Construction Standard LBN 241-15 "Internal Natural Gas Installation Pipework"*. Latvijas Vestnesis. Available at https://likumi.lv/ta/en/en/id/275009
16. Latvian National Code EN 417:2015 Design of External Natural Gas Pipeline Systems with Presure 1,6 Mpa (16 Bar).
17. Latvian National Code EN 419 Internal Gas Pipelines. Installation.
18. Romanovs, A., Tihana, J., & Borodinecs, A. (2019). Impact of hidden defects on the durability and reliability of gas pipelines in cities. In: *IOP Conference Series: Earth and Environmental Science* (pp. 1–12). 27 May–6 June 2019, Moscow, Institute of Physics Publishing. https://doi.org/10.1088/1755-1315/297/1/012046.
19. Latvian National Code No. 445-1:2011. Operation and Maintenance of Natural Gas Distribution and Consumer Supply Systems with Max Operation Pressure 1,6 Mpa (16 Bar). Part 1: General Requirements.
20. Latvian National Code No. 445-2:2011. Operation and Maintenance of Natural Gas Distribution and Consumer Supply Systems with Max Operation Pressure 1,6 Mpa (16 Bar). Part 2: Maintenance Terms, Kinds of Work and the Execution Organization.
21. Selickis, A. (2018). Relocation of the Natural Gas Inlets in Apartment Buildings. *Enerģija un Pasaule, 5* (112), 48–52.

sciendo

LATVIAN JOURNAL OF PHYSICS
AND TECHNICAL SCIENCES
2022, N 5

DOI: 10.2478/lpts-2022-0040

COMPARISON OF PASSIVE AND ACTIVE FIDUCIALS FOR OPTICAL TRACKING

J. Odmins[1], K. Slics[1], R. Fenuks[2], E. Linina[2*], K. Osmanis[1], I. Osmanis[2]

[1] Hansamatrix Innovations Ltd., 1 Ziedleju Str., Marupe, LV-2167, LATVIA
[2] LightSpace Technologies, 1 Ziedleju Str., Marupe, LV-2167, LATVIA
*e-mail: elza.linina@lightspace3d.com

The paper analyses the constraints related to optical tracking of an HMD with a single commercial binocular stereoscopic optical tracking system and offers an overview of different factors affecting the best active fiducial set-up and marker geometries for reliable tracking with a focus on the rotational accuracy of a marker.

Two IR diode models with different emission characteristics were tested as active fiducials and the results were compared to localization accuracy of passive fiducials. In terms of preferable marker geometry, it was found that the area enclosed by the fiducials should be maximized. Thus, due to geometrical constraints, very small marker geometries may not be stable or feasible entirely. Rotational accuracy was analysed for cases when the marker was not directly facing the tracking device and it was found that rotation about one axis introduced errors to the determined orientation in space related to the other axes as well.

Keywords: Active fiducials, angular accuracy, marker geometry, optical tracking, passive fiducials.

1. INTRODUCTION

Augmented reality (AR) devices have been widely researched for the past few decades and are envisioned to penetrate all aspects of everyday life – starting with professional fields such as manufacturing and education, and most notably – the medical field [1]. Even though different implementations of AR already exist [2], the medical field is by far the most demanding in terms of accuracy and comfort of use since surgical procedures can last for several hours. For example, the utilization of an AR headset as a vision aid during surgical procedures puts enormous pressure on the accuracy of image representation [3]. While optics and human perception play a major role in image quality [4], the other side that is equally important for achieving the desired image accu-

racy is object tracking. In this case, it is the tracking of a headset within the real-world space and in relation to the patient and surroundings. The image rendering engine has to rely on accurate position and orientation of the head-mounted display (HMD). Thus, tracking a headset pose accurately is as relevant as providing naturalistic visual cues.

Currently available AR headsets positioned as enterprise-level devices base their pose tracking on visual simultaneous localization and mapping (vSLAM) algorithms, which typically cannot provide the much-needed accuracy in medicine [5]. Depending on the type of task, the preferable image overlay (and consequently, pose tracking) accuracy has to be substantially better than 1 millimetre – although in some scenarios it might be acceptable to achieve lower accuracy [6]. Thus, one of the options is to complement vSLAM with other means of pose tracking or rely on a different tracking solution altogether [7].

One such approach is optical tracking of fiducial markers. This type of object localization within space has long been the go-to method for accurate pose estimation with full 6 degrees of freedom [8]. With the raising popularity of AR devices, research on the topic of pose estimation is still ongoing and many improvements have been made in the past decade [9]–[11]. Based on binocular stereoscopic cameras, commercial optical tool tracking solutions for medical (surgical) settings have been developed [12]. The claimed optical tracking accuracy for tool positioning, for example, during minimally invasive procedures is on the order of 0.1 mm. Better accuracies have been demonstrated by multi-camera setups – for example, with trinocular configuration reaching 0.04 mm [13]. Nevertheless, these very high accuracy values are typically attributed to translation, while in visualization rotational accuracy is similarly important.

Optical tool tracking solutions are already being used in the medical field and many surgical rooms have already been equipped with some type of an optical tracking system. With AR displays offering unprecedented real-time data visualization and thus slowly penetrating the medical field, preinstalled optical tool tracking systems can be repurposed for dual use. The ability to track multiple markers simultaneously also enables the tracking of an HMD with high accuracy – higher than could be achieved by solely relying on vSLAM. Furthermore, utilization of a single tracking device for tools and headset naturally unites coordinate systems, thus alleviating the integration of AR visualizations in medical procedures.

The primary aim of the present research is to analyse the constraints related to optical tracking of an HMD with a single commercial binocular stereoscopic optical tracking system and to develop and verify active fiducial and marker configurations for reliable tracking (putting emphasis on maximizing effective angular range and rotational accuracy).

2. MATERIALS AND METHODS

It should be noted that AR HMDs come in different varieties, including both optically see-through (OST) as well as video see-through (VST) systems [14]. For medical applications OST displays can provide an additional level of safety; nevertheless, fully immersive VR headsets have also been successfully applied and shown as a

valuable addition to the medical professionals [15]. The main feature of a virtual or augmented stereoscopic display is that it provides a sense of 3D depth and thus – an additional layer of spatial awareness to the medical professionals.

Fig. 1. The multifocal HMD prototype system used for tracking experiments.

For the aim of this study, the previously developed prototype system (Fig. 1) is used – a multi-focal OST AR display [16], which provides the user with a 3D image and also matches vergence and accommodation cues, thus providing better eye comfort. While specific geometrical constraints are defined by the layout design of the particular device, general concepts are applicable universally.

Since commercially available AR HMDs were initially oriented towards a wider area of application, including consumer markets, the emphasis was put on ease of use and thus visual simultaneous localization and mapping (vSLAM) as a means of pose tracking. The advantage of vSLAM type tracking is that it can map any reasonably feature-rich environment and provide pose tracking based on the relative position of a headset in respect to the surroundings. Nevertheless, in certain situations the performance can be compromised and overall accuracy is on the order of millimetres. For applications where accuracy is extremely important, vSLAM can be substituted or complemented by depth data derived directly from time-of-flight cameras [17]. It has been shown that complementing a commercial headset with marker-based reference detected by the on-board sensor arrays, the accuracy of pose detection can be reduced to sub-millimetre values [18].

When an HMD system does not house a diverse set of sensors, other approaches have to be utilized. The target pose-tracking accuracies ideally have to be in the order of <0.05 mm for translational motion and <0.05° for the angular localization. Significant effort has been put towards reducing translational errors and the research commonly focuses on translational accuracy while omitting data on angular accuracy. However, for the case of HMD tracking (which means essentially tracking the position of a human head), translational motion is quite uncommon, a much more natural and often occurring motion is rotation. Thus, special attention has to be devoted to achieving accurate and stable tracking of angular changes.

One of the obvious solutions to surgical AR HMD tracking is the utilization of existing navigation systems that have been already adapted for tool tracking [19]. These are designed to visualize tool tips beyond their visibility within the human body during, for example, minimally invasive procedures. The precise localization of the tool tip is based on rigid and known geometry of the tool and a precisely defined optical marker comprised of several fiducials (typically 3–6 fiducials). Fiducials are tracked by a system of precisely intercalibrated stereoscopic cameras to derive essential coordinates of a fiducial within a 3D space, including the orientation.

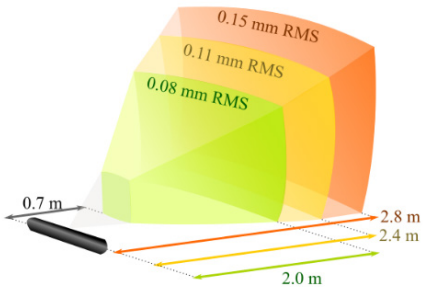

Fig. 2. Atracsys fusionTrack 500 accuracy (pose RMS) for different working distances.

Overall, it would be convenient to utilize a common optical tracking system for the simultaneous tracking of both the HMD and the surgical tools. Thus, this study focuses on marker development and performance evaluation of AR headset tracking using medical stereoscopic tool tracking system *Atracsys FusionTrack 500*.

The Atracsys fusionTrack 500 is a real-time optical pose-tracking system that can track markers in real-time video streams. The fusionTrack is composed of two cameras that observe fiducials simultaneously, and uses triangulation to calculate the locations of these fiducials with a measurement rate of 335 Hz [20].

Atracsys FusionTrack 500 specifications:
Resolution: 2.2 Mpix
Refresh rate: 335 Hz
Working distance: 0.7 to 2.8 m (Fig. 2)

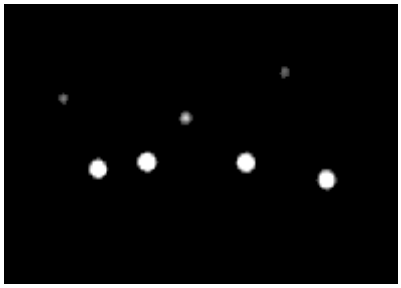

Fig. 3. Comparison of reflectivity as detected by Actracsys FusionTrack 500 for passive fiducials: out of package (bottom row) and after extended handling (top row).

Atracsys FusionTrack 500 and similar systems are designed to work with passive as well as active markers. The camera system is equipped with infrared emitters placed around both camera lenses that are intended for the illumination of retroreflective fiducials. Most commonly, retroreflective fiducials are either flat circles or three-dimensional spheres that are highly visible to the infrared cameras. Spherical fiducials are considered more versatile – as they can be observed from larger angles; nevertheless, for tool tracking flat fiducials perform equally well. Unfortunately, in the setting of surgery, passive markers are subject to contamination and loss of reflectivity (Fig. 3), which interferes with robust pose tracking. Generally, retroreflective fiducials are treated as consumables and changed during set time intervals or upon need.

An alternative to the retro-reflective spheres or disks is the use of active markers comprised of infrared (IR) light emitting diodes (LEDs) whereby a pattern of LEDs is arranged on a rigid structure associated with a tool or a headset. While this approach ensures a more robust overall tracking (mostly due to LEDs not being as prone to contamination as the large-surface passive markers), there are other challenges that often place IR LEDs at a disadvantageous position.

IR LEDs require electrical power to provide tracking capability, which means a battery or some other power-source needs to be associated with the active marker. For tool tracking, this adds to the weight and can make a tool more difficult to use. For a battery or accumulator-type power source, some monitoring is also necessary as it can be detrimental to the health of a patient if a procedure has to be stopped midway to change an empty battery.

For HMDs the use of active markers can be justified more easily as the additional

weight of LEDs is just a small fraction of the total weight of such a device; however, power consumption can still cause issues. Small form-factor LEDs can be driven with up to 100 mA of current, which adds up to about a 100 mW. A marker is typically comprised of 3 to 6 LEDs that can be a considerable number if the device is battery-powered. In tethered devices, power consumption might not be the primary concern; however, the dissipated heat is a prominent issue, as it can interfere with the comfort of wearing an HMD and can negatively affect the performance of embedded semiconductors such as microcontrollers, processors, FPGA chips, etc. [21].

3. RESULTS AND DISCUSSION

3.1. Fiducial Analysis

Atracsys FusionTrack 500 is designed to work well with different types of passive markers. For this purpose, retroreflective spheres (Navigation Markers produced by ILUMARK) of 12 mm in diameter were chosen as a reference for making comparisons between different active IR LED fiducials. Due to the limited resolution of the cameras, any fiducial needs to reach a certain size threshold reported by the camera sensor to be recognised as a fiducial. In the case of IR LEDs as active markers, the reported size is a function of both the driving current of an LED and the physical distance to it. With the default image acquisition and processing parameters, different LEDs (in terms of emitter size and consumed power) were tested by varying the forward current, distance from the camera system, and tilt angle of LEDs with respect to the camera system. Additionally, the tracking jitter of a stationary fiducial in relation to its size (controlled by current) and distance was also determined.

Two IR LEDs from Osram – SFH 4250-S and SFH 4053 – were investigated and compared to the passive markers. The SFH 4250-S was endorsed by developers of the tracking system, while the SFH 4053 was chosen due to the relatively small package and high brightness. The main differences are due to the emitter size and emission angle. The key characteristics of both LEDs are shown in Table 1.

Table 1. Comparison of the Main Parameters for IR LEDs Produced by Osram – Models SFH 4250-S and SFH 4053

	SFH 4250-S	SFH 4053
Centroid wavelength, nm	850	850
Maximum forward current, mA	100	70
Emission half angle, °	60	70
Active chip area, mm^2	0.3×0.3	0.2×0.2
Total radiant flux, mW	100	35
Radiant intensity, mW/sr (at I_f max)	18–28	4.5–11.2
Package	PLCC-4 (3.65 mm×2.95 mm×2.15 mm)	0402 (1 mm ×0.5 mm×0.45 mm)

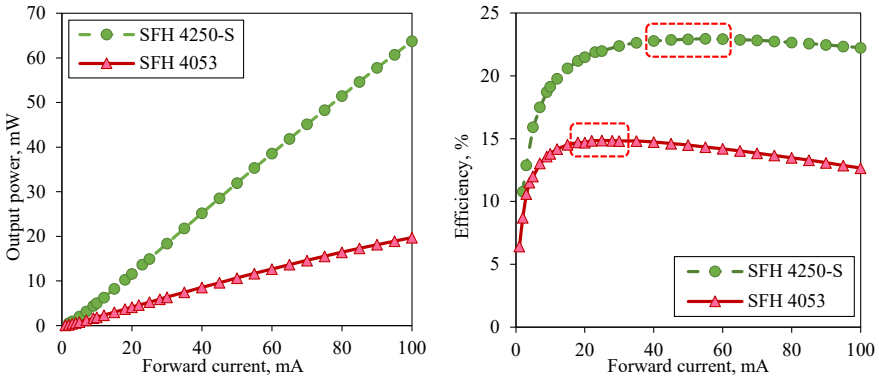

Fig. 4. **Left:** Output power of SFH 4250-S and SFH 4053 LEDs as a function of driving current. **Right:** Efficiency of SFH 4250-S and SFH 4053 LEDs as a function of driving current.

Due to the fact that electronic components often vary in bins and manufacturer datasheets are provided only for reference values, the actual optical output power and efficiency of both LEDs were determined (Fig. 4) experimentally.

The measurements were carried out using the *Agilent Technologies 3606A* power supply in constant current mode. The voltage values were read from the built-in voltmeter. The output power was measured by *Thorlabs PM400* in conjunction with the *S146C integrating sphere* sensor.

It can be noted that from the efficiency standpoint, the best performance from the SFH 4250-S LED can be expected for forward current in the range from about 40 mA to 60 mA, whereas for SFH 4053 the same is true for the 18 mA to 30 mA range. In terms of absolute efficiency, the SFH 4250-S is superior.

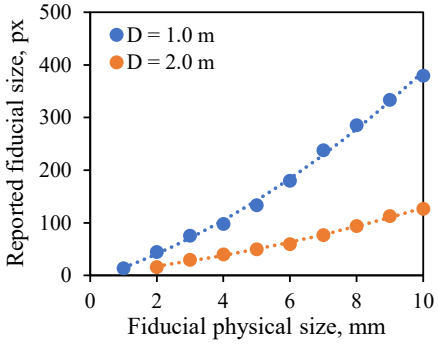

Fig. 5. Atracsys FusionTrack 500 reported fiducial size in pixels at physical distances of 1.0 and 2.0 m for different-sized passive flat disk markers.

A passive retroreflective fiducial forms a predictable response signal on the image capturing sensors of *FusionTrack 500* system – there is a direct correlation between the number of activated pixels and the physical size of the fiducial (Fig. 3).

However, for active LED-based fiducials this is not as straight forward – the reported size varies with both the distance (Fig. 6 (right)) and the forward current used to drive the LED (Fig. 6 (left)).

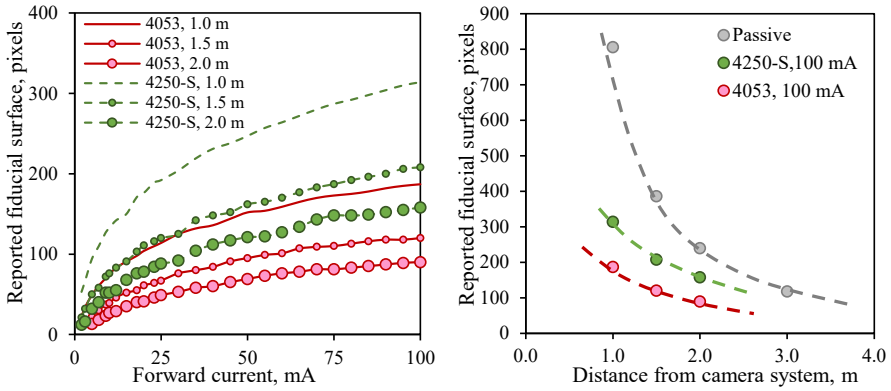

Fig. 6. **Left**: the reported fiducial surface area for SFH 4250-S and SFH 4053 LEDs at different distances and with different driving currents. **Right**: the reported fiducial size as a function of distance to the camera system at maximum driving current with passive marker data (ILUMARK, 12 mm) for reference.

For reliable detection, the activated area on the camera sensor has to be large enough to be recognised as fiducial. By default, it is set to 40 pixels. As it can be seen, the standard passive fiducial balls at relevant working distances of 1.5 m and 2.0 m result in a relatively large signal – approximately 400 pixels and 240 pixels, respectively. In contrast, the LEDs driven at maximum forward current for the same distances of 1.5 m and 2.0 m can achieve only almost half that – 200 and 160 pixels, respectively.

At this driving current of 100 mA, a single LED consumes almost 0.29 W and it would amount to at least 1.16 W total power consumption for a typical 4-fiducial marker in continuous driving mode. A lot of this power is dissipated as heat, which can influence the performance of the LEDs themselves as well as be inconvenient to the user. The focus further is thus on the accuracy and consistency of detection for different driving currents (as related to the size detected by the cameras). For this purpose, different fiducials were rigidly fixed in relation to the tracking camera system and series of registration frames were accumulated alongside with complementary data about the registered coordinates of a fiducial. For LED markers, the relevant current range – between 20 and 100 mA – was analysed (Figs. 7 and 8).

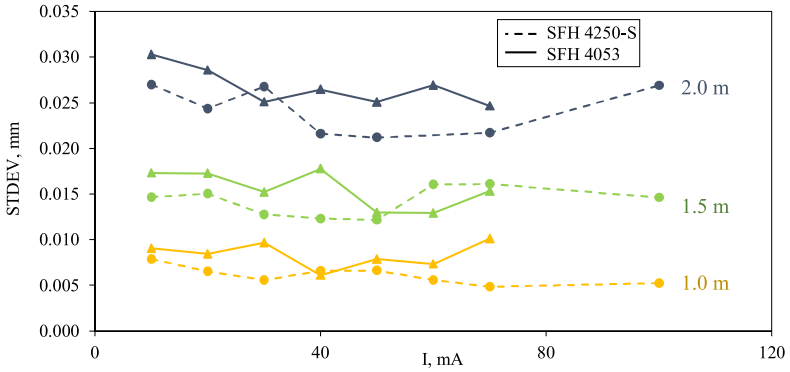

Fig. 7. Comparison of active fiducial (IR LEDs SFH 5042-S and SFH 4053) localization accuracy at different distances to the camera system for varying driving currents (20 mA to 70 mA and 20 mA to 100 mA, respectively).

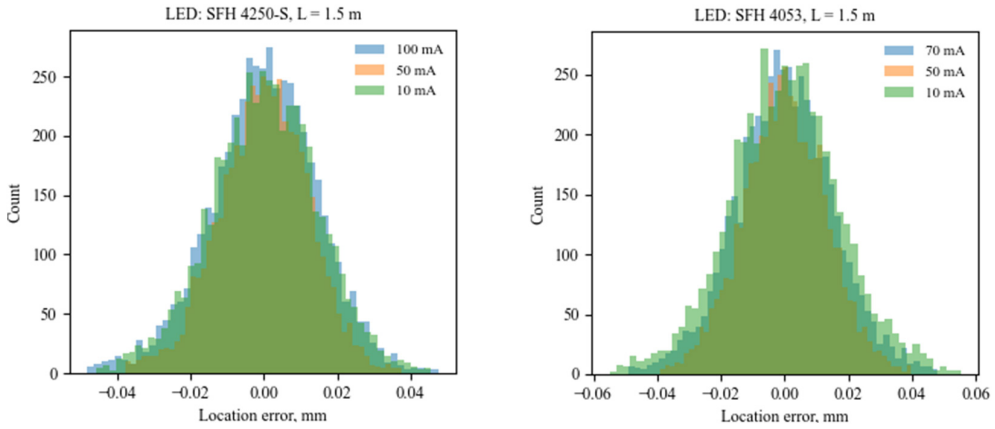

Fig. 8. **Left**: Distribution of the determined coordinate values around the mean for SFH 4250-S at 1.5 m distance from the camera-system (shown for 10, 50 and 100 mA driving current). **Right**: Distribution of the determined coordinate values around the mean for SFH 4053 at 1.5 m distance from the camera-system (shown for 10, 50 and 70 mA driving current). The FWHM of these distributions are shown in Fig. 7.

The registration error overall follows a normal distribution. It was found that, generally, when the fiducials are above the critical limit for detection, no distinct relation between the dispersion of data and the fiducial size (or rather, the current) could be found. On a small scale in consecutive time intervals during which the supposed ambient conditions – most notably vibrations – were at similar levels, some dependence on the size can be distinguished. These differences, however, are well below the claimed accuracy levels of the tracking system and essentially negligible. Thus, the use of smaller driving currents can easily be justified.

3.2. Marker Construction Analysis

A marker is a rigid array of multiple fiducials. To determine the orientation of a marker, it must be comprised of at least three non-aligned fiducials [22]. Generally, for best possible results, the designed geometry should not have any axes of symmetry and the distances between any two fiducials should be different.

For improved positional and rotational accuracy, markers are comprised of four fiducials instead of three. This helps reduce the pose data errors as they can result in a jittery image which is very unpleasant and distracting for the user even so far as to become unusable. An example of feasible marker geometry can be seen in Fig. 9.

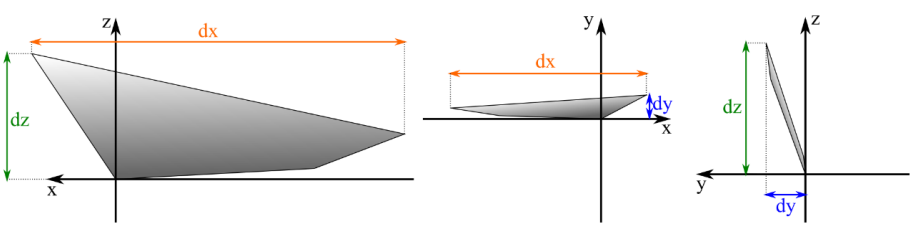

Fig. 9. Sample geometry of a four-fiducial marker. The fiducials are placed at the vertices and form a surface in 3D space.

In order to achieve the best tracking accuracy, the distance between the fiducials has to be large – small displacements of the head then translate into noticeable displacements of the marker fiducials. To achieve good angular resolution (and thus also minimize jitter), the area of the marker should also be maximized as discussed further.

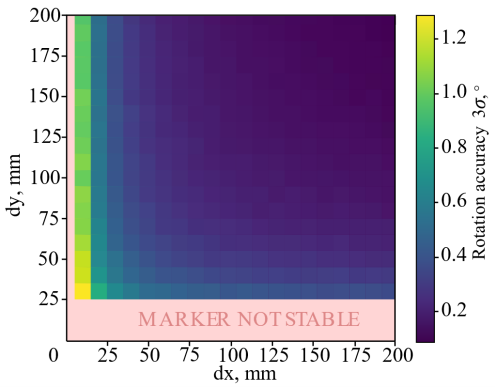

Fig. 10. Rotational accuracy as determined by 3 standard deviations about mean pose of markers with sides of different lengths.

Physically creating and testing different marker geometries is a very time-consuming process. Thus, to determine the best approach, synthetic data were generated and analysed with the *Atracsys Matlab Marker Analyzer*. This tool allows analysing marker geometries (checks segment lengths and symmetries), and can provide the user with expected marker accuracy data. This is achieved by applying the typical noise to the true location of each fiducial and determining the resulting marker location and orientation as if it were detected by the cameras. This process is then repeated to obtain the expected standard deviations of marker location and orientations.

Figure 10 shows the rotational accuracy for markers of different sizes and aspect-ratios – the component is set to be 0 for all markers. Due to the fact that all segments between markers need to be of different lengths (the minimum difference needs to be at least 5 mm), some smaller geometries are not feasible at all or behave in an unstable manner – the rotational errors for markers with mm are well beyond usability. The accuracy here pertains to a marker of a certain geometry placed facing the camera-system.

In real-life scenarios, the marker is rarely if ever positioned face-on towards the camera. Thus, it is important to determine the rotational accuracy of a marker when it is detected by the camera in different orientations. To determine the rotational accuracy of a marker in different orientations, the marker geometry shown in Fig. 11 was rotated about the x-axis, a new marker geometry was defined from this orientation and the obtained marker was again analysed with *Atracsys Matlab Marker Analyzer.*

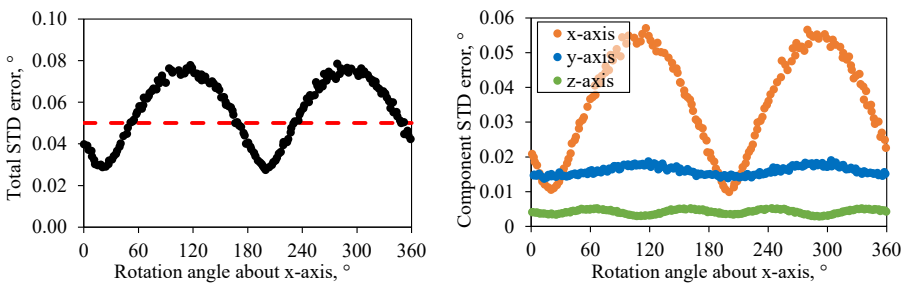

Fig. 11. **Left:** Rotational accuracy of a static marker as a function of rotation angle about the x-axis. The red line denotes the optimal maximum error of 0.05°. **Right:** The rotational accuracy of a static marker as a function of rotation angle about the x-axis separated into components.

As expected, rotating the marker decreases the accuracy with which it can be localized, as the area of the projection on the camera plane becomes smaller (Fig. 11 (left)). However, in Fig. 11 (right) it can be seen that, even though most of the error is related to x-axis localization, rotating the marker about one axis introduces additional location errors for other axes as well.

4. CONCLUSIONS

For the investigation, *Atracsys fusionTrack 500* unit for optical pose tracking was used. Initial tests were also performed with the *Atracsys spryTrack 300*; however, the tracking accuracy of *Atracsys fusionTrack 500* was superior. Thus, it was the unit chosen for further measurements and as the base instrument for synthetic data constraints. Two types of IR diodes were tested as active markers – the SFH 4053 and SFH 4250-S – both produced by Osram. The SFH 4250-S was found to be more energy-efficient and slightly better in terms of fiducial localization accuracy. However, the SFH 4250-S has a larger package and consumes more power overall, while the improvement in localization accuracy is marginal.

To obtain the best possible angular accuracy when locating a marker, the area enclosed by the fiducials should be maximized. This, however, is limited by the available surface area of the HMD and occlusion also becomes an issue. Passive markers can easily be placed on antennae-like protrusions; however, this is more difficult with active markers and the rigidity of the system can be challenging to achieve (and often adds unwanted weight to the HMD). A possible solution would be the creation of multi-face markers or the use of multiple markers for the localization of the HMD. However, the available space is still limited by the physical size of the HMD. Alternatively, a multi-camera set-up for high precision applications could be considered, but is likely to be relatively expensive.

In the experiments described above, the LEDs were driven continuously and, due to the comparatively low efficiency of IR LEDs, the heating of an HMD with a large number of fiducials might be unpleasant for the user. This could potentially be mitigated by pulsing the LEDs; however, this requires additional efforts from the software side as not to lose accuracy.

ACKNOWLEDGEMENTS

The research has been supported by the Competence Centre of Electrical and Optical Equipment Production Sector of Latvia, project No. 1.2.1.1/18/A/006, study No. 1.16 “Development of an Integrated Electronic Solution for Determining the Position of the Head Display in the Room and Providing Remote Assistance Functionality”.

REFERENCES

1. Khor, W. S., Baker, B., Amin, K., Chan, A., Patel, K., & Wong, J. (2016). Augmented and Virtual Reality in Surgery—The Digital Surgical Environment: Applications, Limitations and Legal Pitfalls. *Annals of Translational Medicine*, *4* (23), 454–454. https://doi.org/10.21037/atm.2016.12.23
2. Mekni, M., & Lemieux, A. (2014). Augmented reality: Applications, challenges and future trends. In: *Proceedings of the 13th International Conference on Applied Computer and Applied Computational Science (ACACOS'14)*, (pp. 205–214). 23–25 April 2014, Kuala Lumpur, Malaysia.
3. Fida, B., Cutolo, F., di Franco, G., Ferrari, M., & Ferrari, V. (2018). Augmented Reality in Open Surgery. *Updates in Surgery*, *70* (3), 389–400. https://doi.org/10.1007/s13304-018-0567-8
4. de Cunsel, S. (2019). Evaluation of Augmented Reality (AR) Displays Performance Based on Human Visual Perception. *Digital Optical Technologies*, 110620V. https://doi.org/10.1117/12.2527613
5. Tang, B., & Cao, S. (2020). A Review of VSLAM Technology Applied in Augmented Reality. *IOP Conference Series: Materials Science and Engineering*, *782* (4). https://doi.org/10.1088/1757-899X/782/4/042014
6. Ahn, J., Choi, H., Hong, J., & Hong, J. (2019). Tracking Accuracy of a Stereo Camera-Based Augmented Reality Navigation System for Orthognathic Surgery. *Journal of Oral and Maxillofacial Surgery*, *77* (5), 1070.e1-1070.e11. https://doi.org/10.1016/j.joms.2018.12.032
7. Welch, G., & Foxlin, E. (2002). Motion Tracking: No Silver Bullet, but a Respectable Arsenal. *IEEE Computer Graphics and Applications*, *22* (6), 24–38. https://doi.org/10.1109/MCG.2002.1046626
8. Nishino, H. (2010). A 6DoF fiducial tracking method based on topological region adjacency and angle information for tangible interaction. In: *Proceedings of the 4th International Conference on Tangible, Embedded, and Embodied Interaction – TEI '10* (vol. 18, p. 253). New York, New York, USA: ACM Press. https://doi.org/10.1145/1709886.1709937
9. Furtado, J. S., Liu, H. H. T., Lai, G., Lacheray, H., & Desouza-Coelho, J. (2019). Comparative Analysis of OptiTrack Motion Capture Systems. *Lecture Notes in Mechanical Engineering*, 15–31. https://doi.org/10.1007/978-3-030-17369-2_2
10. Belghit, H., Bellarbi, A., Zenati, N., & Otmane, S. (2018). Vision-based Pose Estimation for Augmented Reality: A Comparison Study. *ArXiv*, 49413387.
11. Cutolo, F., Mamone, V., Carbonaro, N., Ferrari, V., & Tognetti, A. (2020). Ambiguity-Free Optical–Inertial Tracking for Augmented Reality Headsets. *Sensors (Switzerland)*, *20* (5). https://doi.org/10.3390/s20051444
12. Sorriento, A., Porfido, M. B., Mazzoleni, S., Calvosa, G., Tenucci, M., Ciuti, G., & Dario, P. (2020). Optical and Electromagnetic Tracking Systems for Biomedical Applications: A Critical Review on Potentialities and Limitations. *IEEE Reviews in Biomedical Engineering*, *13* (c), 212–232. https://doi.org/10.1109/RBME.2019.2939091
13. Bi, S., Gu, Y., Zou, J., Wang, L., Zhai, C., & Gong, M. (2021). High Precision Optical Tracking System Based on near Infrared Trinocular Stereo Vision. *Sensors*, *21* (7), 2528. https://doi.org/10.3390/s21072528
14. Ballestin, G., Solari, F., & Chessa, M. (2018). Perception and action in peripersonal space: A comparison between video and optical see-through augmented reality devices. In *2018 IEEE International Symposium on Mixed and Augmented Reality Adjunct (ISMAR-Adjunct)* (pp. 184–189). 16–20 October 2018, Munich, Germany. https://doi.org/10.1109/ISMAR-Adjunct.2018.00063

15. Javaid, M., & Haleem, A. (2020). Virtual Reality Applications toward Medical Field. *Clinical Epidemiology and Global Health*, *8* (2), 600–605. https://doi.org/10.1016/j.cegh.2019.12.010
16. Zabels, R., Osmanis, K., Narels, M., Smukulis, R., & Osmanis, I. (2019). Integrated Head-Mounted Display System Based on a Multi-Planar Architecture, *Advances in Display Technologies IX*, 10942, 51–61. https://doi.org/10.1117/12.2509954
17. Hai-Xia, X., Wei, Z., & Jiang, Z. (2015). 3D visual SLAM with a Time-of-Flight camera. In *2015 IEEE Workshop on Signal Processing Systems (SiPS)* (pp. 1–6). 14–16 October 2015, Hangzhou, China. https://doi.org/10.1109/SiPS.2015.7344992
18. Kunz, C., Maurer, P., Kees, F., Henrich, P., Marzi, C., Hlaváč, M., … & Mathis-Ullrich, F. (2020). Infrared Marker Tracking with the HoloLens for Neurosurgical Interventions. *Current Directions in Biomedical Engineering*, *6* (1), 1–4. https://doi.org/10.1515/cdbme-2020-0027
19. Pérez-Pachón, L., Poyade, M., Lowe, T., & Gröning, F. (2020). Image Overlay Surgery Based on Augmented Reality: A Systematic Review. *Advances in Experimental Medicine and Biology*, *1260*, 175–195. https://doi.org/10.1007/978-3-030-47483-6_10
20. Atracsys. (2017). Data Sheet: fusionTrack 500. Available at https://www.atracsys-measurement.com/wp-content/documents/fTk500-datasheet.pdf
21. Khaleghi, B., & Rosing, T. Š. (2019). Thermal-Aware Design and Flow for FPGA Performance Improvement. *Proceedings of the 2019 Design, Automation and Test in Europe Conference and Exhibition, DATE 2019*, 342–347. https://doi.org/10.23919/DATE.2019.8715183
22. Israel, P. A. J., Carlos, P. O. J., Jorge, Á. S., Saúl, T. A., Emilio, V. S. J., & Susana, V. H. (2014). Design and construction of tools with reflecting-disks fiducials for optical stereo trackers: An afforable technique for navigation tools development. In: *11th International Conference on Electrical Engineering, Computing Science and Automatic Control, CCE 2014*, 5684680. 29 September–3 October 2014, Ciudad del Carmen, Mexico. https://doi.org/10.1109/ICEEE.2014.6978258

sciendo

LATVIAN JOURNAL OF PHYSICS
AND TECHNICAL SCIENCES
2022, N 5

DOI: 10.2478/lpts-2022-0041

POTENTIAL DECAY SIMULATION ON INSULATING FILMS

S. Kasri[1], L. Herous[1], K. Smili[1,2], M. T. Kimour[3], A. Dekhane[1*]

[1] Laboratory of Electromechanical Engineering,
University of Badji Mokhtar,
B.P.12, Sidi Amar, Annaba, 23220, ALGERIA
[2] Higher School of Industrial Technologies,
Safsaf city, BP 218, Annaba, 23000, ALGERIA
[3] Laboratory of Embedded Systems Research (LASE),
University of Badji Mokhtar,
B.P.12, Sidi Amar, Annaba, 23220, ALGERIA
*e-mail: a.dekhane@esti-annaba.dz

Surface potential decay (SPD) of a corona charged polymeric material is a powerful tool to characterise electrical properties such as charge transport, trapping/detrapping and recombination. Over the years, various predictive simulation techniques have been proposed to describe charge transport within the material. Despite recent progress, it appears that there have been a few attempts to theoretically interpret the nature of the charge migration on the insulation surface. The aim of the present paper is to introduce a new technique with differential evolution algorithm (DEA) to reveal the steady state surface potential decay experimental results. Experimental measurement was carried on a thin film of polyethylene terephthalate (thickness: 0.5 mm; surface: 50 mm x 50 mm). The domains of variation of the factors used were respectively: 1000 V to 1800 V; 25 to 55 °C; 50 % to 80 %. The simulation results show that computational modelling and optimization approaches may improve the effectiveness to characterise electrical properties of polymers. More importantly, these studies demonstrate that DEA is effective and performs better than the experimental design method.

Keywords: Differential evolution algorithm, genetic algorithms, polymers, simulation, surface potential decay.

1. INTRODUCTION

Synthetic insulating polymers are widely applied in electrical industry due to their excellent electrical, thermal, and mechanical properties. In many cases, such polymers are used in hostile environments where they may be subjected to attack by non-ionizing radiations, water, corrosive materials, etc. Therefore, their properties are deteriorated and a premature ageing of the electrical insulation can be observed.

The measurement of the isothermal surface potential decay after charge deposition provides a convenient method to investigate the electrical properties of such insulating materials. The main fields of industry source of numerous works on surface potential decay are electro optics (photocopies and laser printers), electret materials and electrical industry for the development of insulating polymers for high voltage insulation [1]–[4].

During the past two decades, many theories have been developed in order to explain the kinetics of surface potential decay. In a previous paper [5]–[8], experimental measurements on 500 mm thick polyethylene terephthalate (PET) samples pointed out that the surface potential decay is influenced by several factors, including the initial potential *V0*, the duration *tc* of the exposure to the corona discharge, the ambient temperature θ, and the relative humidity *RH*.

The design of experiment methodology has been recently used to optimize the process by evaluating instantaneously the effects of some factors and their interactions on the process [9]. Recently, modelling surface potential decay of polymer (PET) by artificial neuron networks [10]–[12] has been employed for modelling this phenomenon. The main objective of the present study is to assess the applicability of a new technique with differential evolution algorithm (DEA) to reveal the steady state surface potential decay experimental results. The novelty of this methodology is that it proposes a factorial experimentation, in which the factors investigated vary simultaneously. Simple mathematical processing of experimental design data enables a rather accurate evaluation of factor effects and interactions. Experimental design can also be used for determining the relationship between the factors affecting a process and the output of that process.

2. EXPERIMENTAL DETAILS

The surface potential decay experiment is described in Fig. 1 [6], [8].

The samples with one surface held firmly on to an earthed metal plate electrode and the other free surface were used. They might be charged on their free surface by exposure to a corona point discharge situated above the surface and behind a grid electrode. The grid was a fine metal mesh situated above the sample surface so that a reasonably uniform field might be generated in the gap between the grid and the PET surface [13], [14].

By selecting an appropriate corona point and grid potential *Vp* and *Vg*, respectively, it was possible to charge the polymer surface with ions of either sign and to a potential value limited by the grid potential *Vg*.

After charging the turntable was rotated under a non-contacting probe. The probe

was connected to an electrostatic voltmeter (Monroe type), which transmitted data to the computer. The surface potential was then measured and continuously recorded. All operations were controlled by a computer.

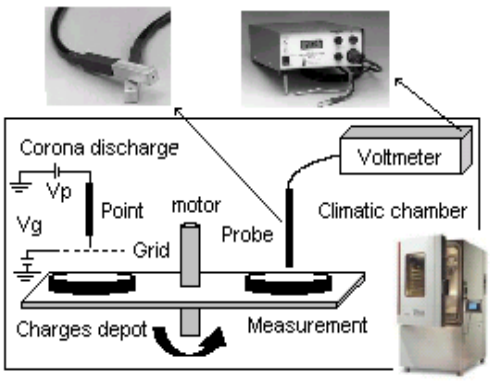

Fig. 1. Equivalent electrical circuit of photovoltaic module.

All the measurements of surface potential decay were carried out in situ, in a commercial climatic chamber, in which humidity and temperature were controlled. Experimental measurement was carried out on a thin film of polyethylene terephthalate (thickness: 0.5 mm; surface: 50 mm x 50 mm). The domains of factors variation used were respectively:

- Initial potential V_0: -1000 to -1800 V.
- Ambient temperature **θ:** 20 to 55 °C.
- Relative humidity RH: 50 % to 80 %.

A typical family of *V(t)* curves obtained [6] after negative corona at various grid potentials, under similar ambient conditions (T= 55 °C, RH= 50 %) can be examined in Fig. 2. A fast-initial decay of the potential can be noticed in all cases, as well as the so-called cross-over phenomenon [15], [16]; the samples initially charged to a higher potential displayed a more rapid potential decay than those charged to a lower potential. The fast-initial decay of the surface potential might be attributed to the partial injection of deposited charges into the polymer bulk under the electrical field generated by the charges themselves, and this trend was enhanced by raising V_0. Once injected into the bulk, the charges are expected to drift towards the ground electrode under the influence of this field. Therefore, the initial potential V_0 has a stronger effect right on the short-term decay rate $D_{500\,s}$ than on the long-term decay rate $D_{3000\,s}$.

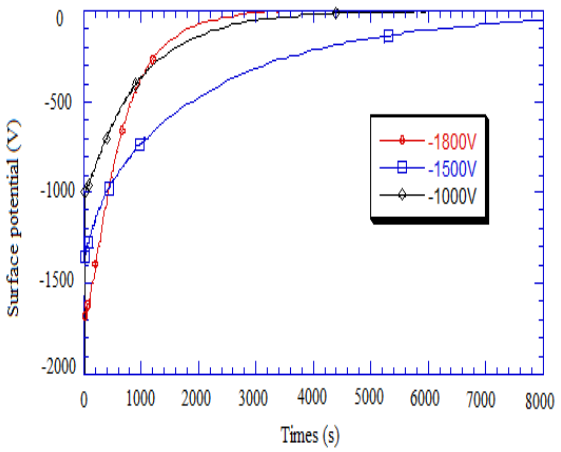

Fig. 2. Surface potential decay curves obtained at three values of the initial potential *V0* at *RH* = 50 % and θ = 55 °C.

The protocol of the experimental tests carried out is described in Table 1 [6].

Table 1. Experimental Test Protocol

	Factors			Responses	
No.	V_0 **(V)**	θ (°C)	***RH*** **(%)**	D_{500} **(%)**	D_{3000} **(%)**
1	-1000	20	50	04.88	20.22
2	-1800	20	50	10.37	29.90
3	-1000	55	50	37.59	94.82
4	-1800	55	50	51.46	99.34
5	-1000	20	80	36.51	89.72
6	-1800	20	80	50.84	97.72
7	-1000	55	80	91.30	100
8	-1800	55	80	99.51	100
9	-1400	37.5	65	45.94	76.64
10	-1400	37.5	65	43.93	76.23
11	-1400	37.5	65	42.92	76.08

3. DIFFERENTIAL EVOLUTION ALGORITHM

As a variant of genetic algorithms, the differential evolution algorithm (DE) is among the most efficient evolutionary algorithms in the field of optimization. DE is an optimization technique that iteratively modifies a population of candidate solutions to converge it to an optimum of your function [17]–[19].

In DE, the solutions are represented as a population of individuals (or vectors). Each individual is represented by a set of real numbers. These real numbers are the values of the parameters of the function to be minimized, which measures the quality of an individual. It is proposed as a simple and powerful population-based stochastic optimization method, which is originally motivated by the mechanism of natural selection. This algorithm searches for solutions using three basic operators: mutation, crossover and greedy selection. Mutation is used to generate a mutant vector by adding differential vectors. After that, crossover operator generates the trial vector by combining the parameters of the mutated vector with the parameters of a parent vector selected from the population. The main difference with genetic algorithms is that it lies in the construction of better solutions where genetic algorithms rely on crossover, firstly, while DE is based on a mutation operation firstly [20]–[23].

Moreover, DE has been proven to be quite efficient when solving real-world problems [24]–[26].

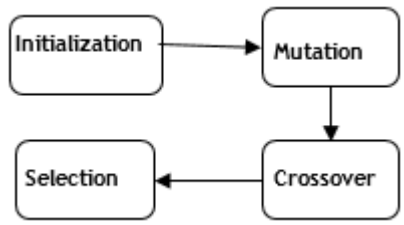

Fig. 3. Block diagram of the DE method.

The main steps of the algorithm are organised according to initializations of the

population, mutation, crossover (recombination), and selection (see Figs. 3 and 4). These operations are applied for minimizing the function f_{obj}.

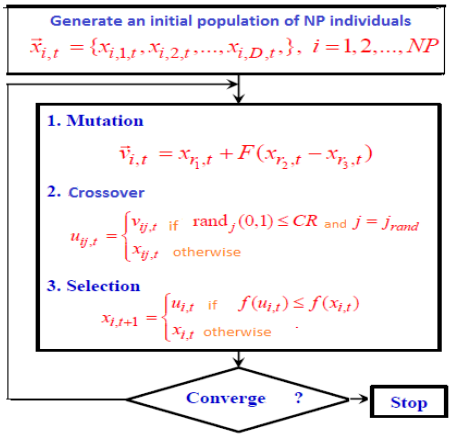

Fig. 4. DE algorithm scheme.

- **Step 1:** We start by generating an initial population where each individual represented by a vector is a candidate solution and its elements are randomly generated, while ensuring compliance with the constraints.
- **Step 2:** A mutant vector is produced $V_{i,t}=x_{r1,t}+F(x_{r2,t} - x_{r3,t})$, where $x_{r1,t}$, $x_{r2,t}$, $x_{r3,t}$, are three candidate solution vectors, distinct, chosen at random among the individuals of the population. F is a random variable $\in$ [0,2].
- **Step 3:** Vector components between X and V are randomly permuted to produce a test vector U. At least one component of V must be exchanged.
- **Step 4:** X is replaced in the population by U only if it is a better candidate (i.e., it better optimizes the "objective" function).

3.1 Improved DE Algorithm

The standard DE algorithm suffers from the fact that it easily falls into the local optimum. In order to get around this problem, we advocate two aspects of modification.

The first aspect concerns the diversification of the initial population through the introduction of the chaotic system concept. The second aspect not only improves diversification but also speeds convergence. Conclusive tests and evaluations were performed on benchmark functions [18].

The first aspect of our proposal is to introduce the concept of Chaos [27], [28]. Chaos has the property of non-repetition and for that it looks for the best solution faster than any search strategy that depends on the probability distribution. It also has a property of ergodicity. The chaotic sequence shows a property of ergodicity that facilitates research. We use a logistic equation to produce the initial population. The logistic mapping equation is as follows:

$$x_{m+1,n} = \mu x_{m,n}\left(1 - x_{m,n}\right) \quad (1)$$

(n=1.2…N ; m = 1.2…M),

when

$x_{m,n} \in [0,1]$ and $0 < \mu \le 4$, the system is at the chaotic state.

$x_{m,n}$ is transformed according to Eq. (1) in order to construct the initial population with a size equal to M and a dimension equal to N.

$$x_{m,n} = L_n + x_{m,n}(U_n - L_n)\,, \quad (2)$$

where

U_n and L_n are respectively the upper limit and the lower limit of the variables or individuals in the n^{th} dimension. The production of a uniform population using logistical chaos mapping can improve the efficiency of the algorithm search.

The second aspect relates to the introduction of a crossing operator that combines

the target vector X with the mutant vector V, according to the following formula:

$$E = \alpha * V_i + (1-\alpha)*X_i, \quad (3)$$

where
$\alpha \in [0,1]$.
At the moment of selection, we took the best individual.

4. PROBLEM FORMULATION

The aim of the study is to find the best coefficients of our polynomial which represents the rate of surface potential decay of PET polyethylene. The linear model of the system response is a polynomial of the first degree, where the response of this process is expressed according to three factors.

$$x_i = V_0^*;\ x_2 = \theta^*;\ x_3 = RH^*$$

$$y = a_0 + a_1 V_0^* + a_2 \theta^* + a_3 RH^* + a_{1,2} V_0^* \theta^* + a_{1,3} V_0^* RH^* + a_{2,3} \theta^* RH^* + a_{1,2,3} V_0^* \theta^* RH^* \quad (4)$$

where
y – the answer or the magnitude of interest. It is measured during the experiment and is obtained with a given precision;
a_0 – the predicted value of the response to the experimental domain centre;
a_i – the factor effect of x_i;
a_{ij} – interaction between factors x_i and x_j;
a_{ijk} – interaction between factors x_i, x_j, x_k.

4.1 The Objective Function (f_{obj})

The "objective" function, or fitness, associates a value for each individual. This value is intended to assess whether an individual is better suited than another to the environment. This means that it quantifies the answer provided to the problem for a given potential solution.

This function depends on the error between the predicted output of the model and the measured experimental value, it is defined by the following relation:

$$Fobj = \frac{1}{N} \sum_{1}^{N} (| y_i - y_{mes} |) \quad (5)$$

where
N – the number of experimental tests;
Y_i – the answer predicted by the model;
Y_{mes} – the measured answer.

4.2 Initialization

The first step of this algorithm is the creation of a population composed of individuals of determinate size. At first, the algorithm initializes individuals by generating random values for each coefficient within given limits.

4.3 Evaluation

At this stage, we have our initial population of 40 vectors and we can now evaluate them using our f_{obj}. Although these vectors are random points in the function space, some of them are better than others. After evaluating these random vectors, we can see the vector that is the best of the population, with minimal f_{obj}, so these values should be closer to those we are looking for.

4.4 Mutation and Recombination

We present here how the algorithm can find a good solution from this set of random values. For each vector X of the population, we take from the population randomly three other vectors: x_{r1}, t, x_{r2}, t, x_{r3}, t. We start with the first initial population vector (called the target vector), and in order to select x_{r1}, t, x_{r2}, t, x_{r3}, t, we first generate a list with the indices of the vectors of the population, excluding the current vector (j = 0); we create a mutant vector combining x_{r1}, t, x_{r2}, t, x_{r3}, t, by calculating the difference between x_{r2}, t and x_{r3}, t by adding these differences to x_{r1}, t after multiplying them by a random mutation factor belonging to l interval [0,1]. A larger mutation factor increases the search radius but may slow the convergence of the algorithm.

In the recombination step, an assay vector composed of a mixture of elements from the mutant vector V and the vector X is created. This is done by changing the elements at certain positions of the current vector with those of the mutant vector.

For each position, we decide (with a probability defined by recomb) whether this element will be replaced or not by that of the mutant at the same position. To generate the crossing points, it is enough to generate uniform random values $\in$ [0, 1] and to check if the values are lower than recomb. After generating our new test vector, we need to evaluate it to measure its quality. If this test vector is better than the target vector X, we replace it with this test vector.

Iteration is accomplished when all vectors of the population have been processed. A certain number of iterations are executed. After every iteration, the best overall solution is determined. At the end of the processing, the vector representing the best overall solution gives the optimal coefficients that minimize the "objective" function.

5. RESULTS

Our approach to solving the problem is based on the improved version of the differential evolution algorithm that we implemented under Python 3.7, using the parameters in Table 2.

Figure 5 illustrates the evolution of the selective function of the best individual for the two time intervals (D_{500s}) and (D_{3000s}). We see a rapid convergence towards the optimal solution.

In addition, we highlight good accuracy of the solution in that the error rate is low (2.77428 % and 1.79136 %).

Table 2. Parameters of DE

Parameters	**Value**
Iteration number with D_{3000}	7000
Iteration number with D_{500}	4000
NP: individual number	40
mutate: probability of the	0.8
recomb: probability of the crossover	0.6

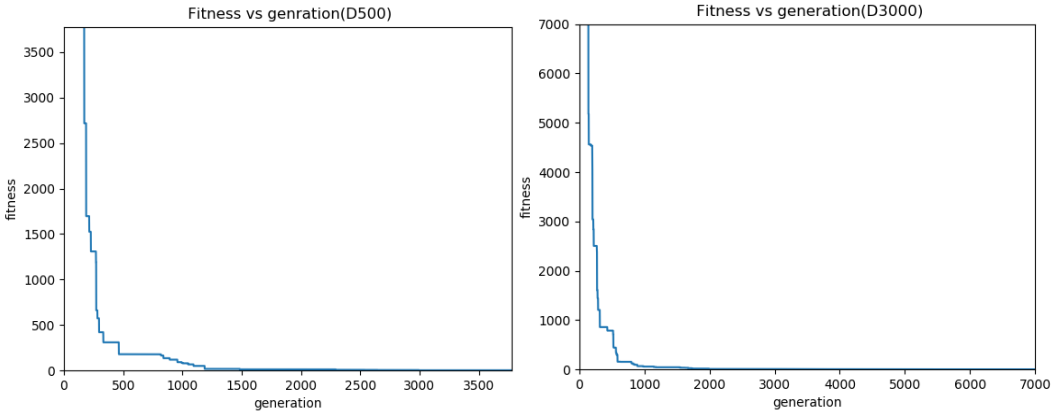

Fig. 5. Evolution of the value of f_{obj} according to the number of generations (D500s) and (D3000s) using DE.

Once the coefficients are determined, the following mathematical models are established:

$$D_{500}= 28\ .613165+0.056946\ V_0^*-2.259979\Theta^*-0.656613RH^*-0.00163\ V_0^*\Theta^*-0.001041\ V_0^*\ RH^*+0.052016\ \Theta^*\ RH^*+2.4^{e-05}\ V_0^*\ \Theta^*\ RH^* \quad (6)$$

$$D_{3000}=49.651061+0.099568V_0^*+1.969208\Theta^*+1.237311RH^*-0.00222\,V_0^*\Theta^*-0.001578\,V_0^*RH^*-0.012898\ \Theta^*\ RH^*+3.4^{e-05}\ V_0^*\ \Theta^*\ RH^* \quad (7)$$

Examination of the coefficients of the two polynomial models in the two time intervals shows that the effect of the initial potential factor is less important in relation to the factors: temperature and relative humidity. These have a significant effect on the rate of SPD.

Figure 6 shows iso-response SPD rate curves (D_{500s}, D_{3000s}) as a function of temperature and relative humidity, at V_0 = -1400V, highlighting the important role of these factors and the role of the interaction between them.

This figure shows the importance of temperature and humidity effect on the SPD. It is clear that the two parameters act on the same phenomenon but differently. The effect of temperature appears during the first moments of the decay while the effect of humidity is more widespread over time. The mobility of the electrons strongly depends on the temperature, hence, the appearance of the injection phenomenon from the first moments. This can mean that the action of humidity intensifies the SPD, while the temperature accelerates it.

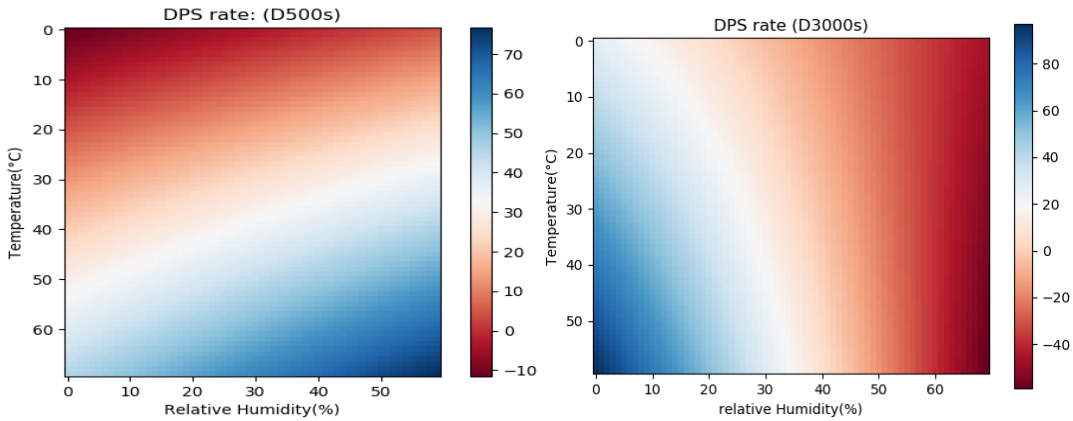

Fig. 6. SPD rate predicted by DE as a function of temperature and the relative humidity RH:(D500 s) and (D3000 s).

Moreover, the predicted response curves computed with Eqs. (6) and (7) and represented in Figs. 7 and 8 can also determine the influence of each factor on the response by plotting the variation of the responses according to the factors. In each case, the other two variables are held constant and equal to their central values V_0 = -1400 V, Θ = 37.5 °C, *RH* = 65 %.

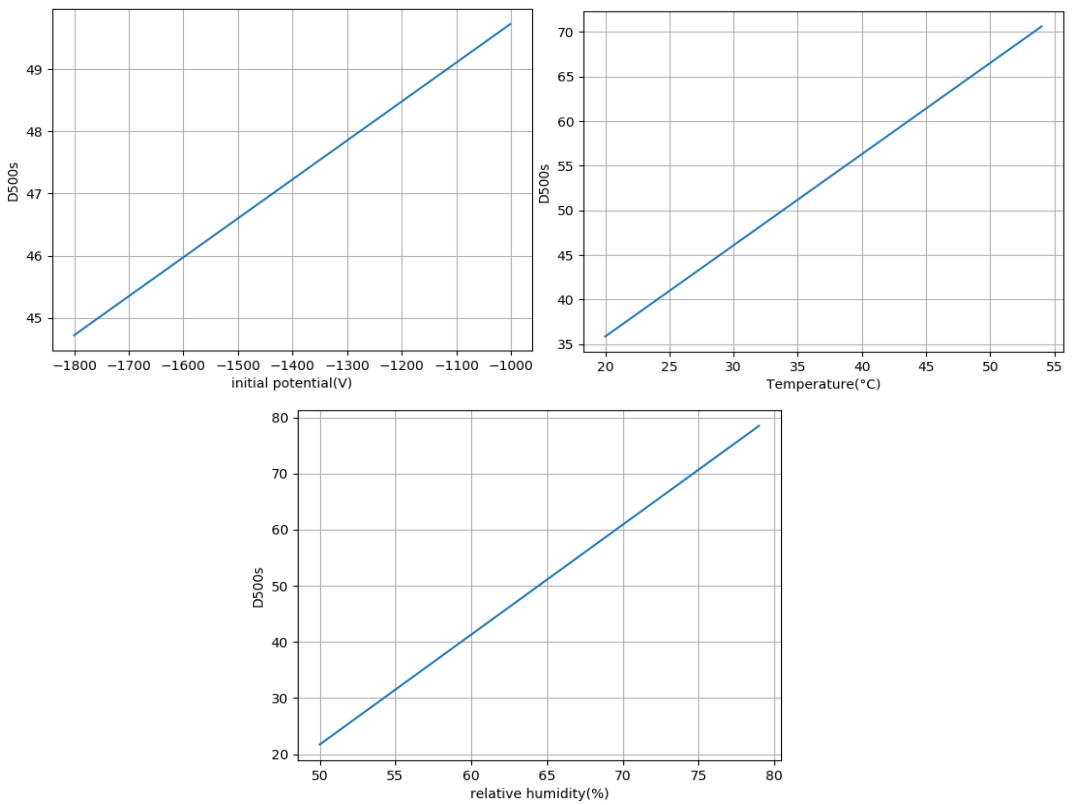

Fig. 7. Predicted responses (D500) with DE according to factors: *V0* and *RH*.

If we consider the effect of each factor on the DPS rate, we note that the fall is very important, it depends strongly on the temperature and the relative humidity for the first linear model, D_{500s} (see Fig. 7).

This behaviour can be explained by the fact that at the first moment of measurements the high decay rate and consequently the high sample unloading speed can be attributed to the charge injection mechanism. The injected charges are subject to the local field, which will drive them towards the rear face. In the long term D_{3000s} (500s–3000s) (Fig. 8), it seems that the effect of both factors whether it is temperature or relative humidity on the DPS becomes less important than the short term D_{500s}.

It is also important to note that the recorded surface potential decline is more significant, especially in the first moments of measurement (~ 500s). For long periods, a very slow or even stationary decline is observed, it is possible that the charges do not have enough energy to be injected into the volume of the material. The deep states of the surface permanently trap part of the deposited charge.

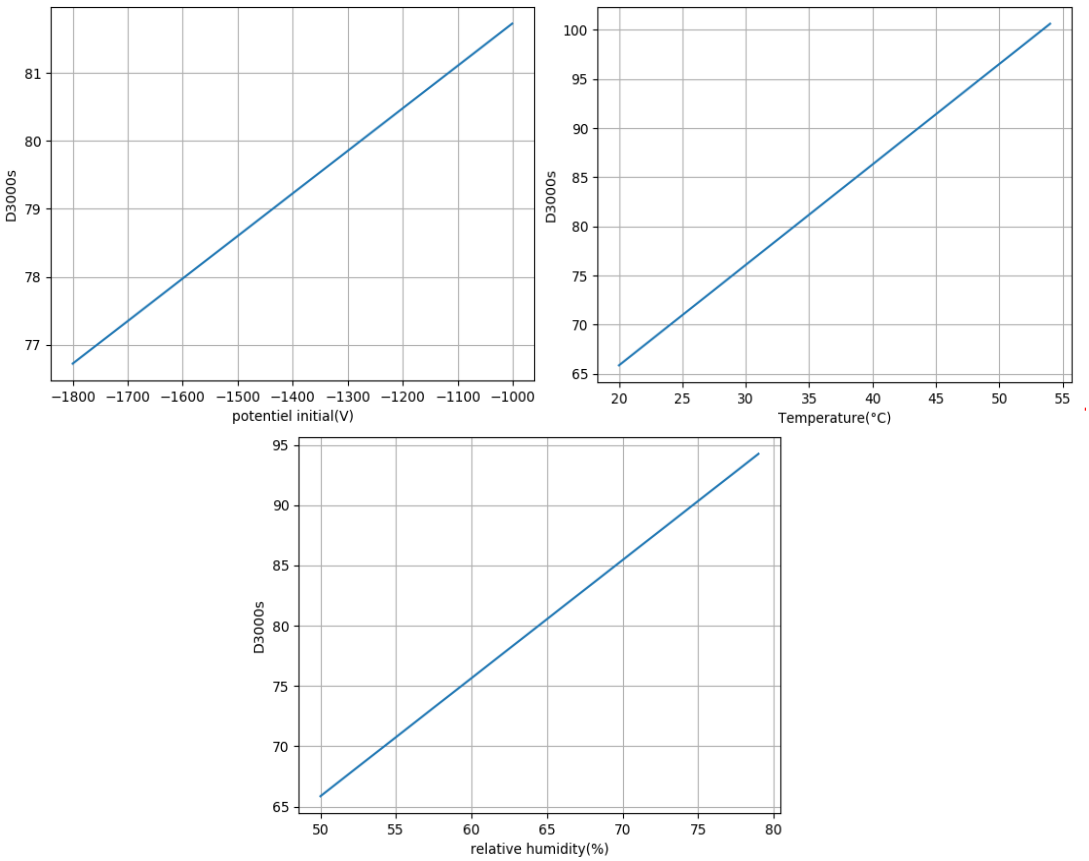

Fig. 8. Predicted responses (D3000) with DE according to factors: (*V0*, and *RH*).

6. VALIDATION

Let us recall that we divided the experimental data set into two parts: the first part, which represents 80 %, was used for the determination of the coefficients by the improved differential evolution algorithm (DEA). The remaining 20 % was used to validate our model. By replacing the three factors in the found mathematical models, one calculates the rate of decline D_t of the corresponding (D_{500s} and D_{300s}), then one compares it with the experimental one. The results obtained (see Table 3) show a very slight difference, which signifies a very good quality of the results obtained and hence the efficiency of our algorithm that improves differential evolution optimization method. Therefore, both models fit well the experimental data, and enable accurate prediction of the surface potential decay rate.

Compared to the results obtained by genetic algorithms, it is quite clear that the improved differential evolution algorithm more accurately determines the rate of potential decay for the two periods D_{500s} and D_{3000s}.

In order to show the superiority of our approach, we compared the results obtained by applying genetic algorithms with those obtained by our technique. This superiority is materialized as much by the execution time as by the precision of the results. Table 4 illustrates this comparison.

Table 3. Validation Results of Mathematical Models with DE

	Predicted value	Experimental value	Precision	Excution time
$\mathbf{D_{500}}$	44.52516	45.94	0.9692	52 s
$\mathbf{D_{3000}}$	73.08340	76.64	0.9535	95 s

Table 4. Validation Results of Mathematical Models with GA

	Predicted value	Experimental value	Precision	Execution time
$\mathbf{D_{500}}$	38.87431	45.94	0.8461	112 s
$\mathbf{D_{3000}}$	67.33452	76.64	0.8806	185 s

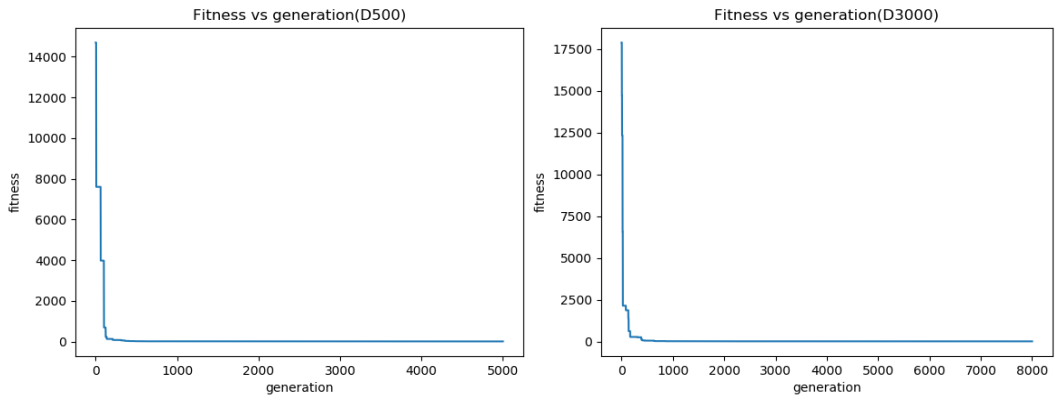

Fig. 9. Evolution of the value of f_{obj} according to the number of generations (D500 s) and (D3000 s) obtained by GA.

Figure 9 illustrates the evolution of the "objective" function by the number of generations. It shows that in the short term (D_{500s}) the genetic algorithm reaches the best solution in the 1500 generation after 112 s. In the long term (D_{3000s}), the algorithm reaches the best solution at the 3200 generation after 185 s; this is much compared to that obtained by our DEA algorithm.

7. CONCLUSION

Applications in electrical engineering use insulation systems that are often a limiting factor in performance, especially for service life or voltage withstand; hence, they need to be improved and there should be an opportunity to predict their lifetime.

In this study, we defined the mathematical model of SPD characterisation, to which we applied the improved and adapted differential evolution algorithm. It allowed not only quantifying the effect of each factor but also determining the interaction between them. The developed algorithm has a great flexibility of use and may handle large problems. It has been proven powerful for optimizing complex functions and can work well in problems where other techniques cannot be used.

Compared to the genetic algorithm, it exhibited lower computation time than that of the genetic algorithm. Moreover, it allows for a better result in terms of precision and estimation of the coefficients of the mathematical models for the problem of the decline in surface potential.

This leads to the belief that in the future our modified version of the differential evolution algorithm will be able to solve problems related to modelling and optimization of experimental work with increased complexity (non-linearity).

REFERENCES

1. Moreno, R.A., & Gross, B. (1976). Measurement of Potential Buildup and Decay, Surface Charge Density, and Charging Currents of Corona-Charged Polymer Foil Electrets. *J. Appl. Phys., 47* (8), 3397–3402.
2. Batra, I.P., Kanazawa, K.D., & Seki, H. (1970). Discharge Characteristics of Photoconducting Insulators. *J. Appl. Phys., 41* (8), 3416–3422.
3. Vance, D.W. (1971). Surface Charging of Insulators by Ion Irradiation. *J. Appl. Phys, 42* (13), 5430–5443.
4. Young, R.H. (1992). Kinetics of Xerographic Discharge by Surface Charge Injection. *J. Appl. Phys*, *72* (7), 2993–3004.
5. Ieda, M., Sawa, G., & Shinohara, I. (1967). A Decay Process of Surface Electric Charges across Polyethylene Film. *Japan. J. Appl. Phys, 6*, 793–794.
6. Herous, L., Nemamcha, M., Remadnia, M., & Dascalescu, L. (2009). Factors that Influence the Surface Potential Decay on a Thin Film of Polyethylene Terephthalate (PET). *Journal of Electrostatics, 67*, 198–202.
7. Herous, L., Remadnia, M., Kachi, M., & Nemamcha, M. (2009). Decay of Electrical Charges on Polyethylene Terephthalate Surface. *Journal of Engineering Science and Technology Review, 2* (1), 87–90.

8. Smili, K., & Herous, L. (2019). Corona Charging and Charge Decay on Polyethylene Terephthalate Films (PET). *Electrotehnica, Electronica, Automatica (EEA), 67* (3), 81–90. ISSN 1582-5175.
9. Remadnia, M., Nemamcha, M., Herous, L., & Dascalescu, L. (2011). Decay of the Electrical Potential at the Surface of Corona Charged Uniforms Layers of HIPS Granules. *IEEE Transactions on Dielectrics and Electrical Insulation, 18* (2), 579–587.
10. Kasri, S., & Herous, L. (2018). Neuronal approach for estimating surface potential decay in polyethylene terephthalate. In: Proceeding of the 3rd International Conference on Technological Advances in Electrical Engineering (ICTAEE'18), (pp. 392–397). 10–12 December 2018, Skikda, Algeria.
11. Kasri, S., & Herous, L. (2018). Modeling the potential surface decay of a polymer (PET) using artificial neural networks. In: Proceeding of the 4th International Organic Chemistry Days, (p. 180). 1–3 December 2018, ANNABA, Algeria.
12. Mizutani, T., Oomura, T., & Ieda, M. (1989). Surface Potential Decay in Polyethylene. *Japan. J. Appl. Phys, 20*, 855–859.
13. Rougdia, K., Herous, L., Fatihou, A., Tabti, B., Nemamcha, M., & Dascalescu, L. (2015). Experimental Modelling of the Electric Potential Decay at the Surface of Polypropylene. *Journal of Electrostatics, 76*, 262–267.
14. Rouagdia, K., Nemamcha, M., Herous, L., Dascalescu, L., & Mellouki, H. (2015). Surface Potential Decay of DC-corona-charged PET Films on Humid Electrodes. *Journal of Electrostatics, 78*, 17–21.
15. von Berlepsch, H. (1985). Interpretation of Surface Potential Kinetics in HD-PE by a Trapping Model. *J. Phys. D: Appl. Phys., 18*, 1155.
16. Llovera, P., "Study of charge injection mechanisms in insulating materials by means of electrostatic measurements of potential decline and return, New analysis tools ", thesis PhD University of Paris XI Orsay, 2002.
17. Price, K. V., Storn, R. M., & Lampinen, J. A. (2014). *Differential Evolution: A practical Approach to Global Optimization*. Springer.
18. Derviş, K., & Selçuk, Ö. (2004). A Simple and Global Optimization Algorithm for Engineering Problems: Differential Evolution Algorithm. *Turkish Journal of Electrical Engineering and Computer Science (TUBITAK), 12* (1), 53–60.
19. Storn, R., & Price, K. (1997). Differential Evolution - A Simple and Efficient Heuristic for Global Optimization over Continuous Spaces. *Journal of Global Optimization*, 341–359.
20. Huanzhe, L., Kungi, L., & Xia, L. (2010). A Comparative Study of Artificial Bee Colony, Bees Algorithm and Differential Evolution on Numerical Benchmark Problems. *Appl Math Comput., 107*, 198–207.
21. Canessa, E., & Chaigneau, S. (2017). Response Surface Methodology for Estimating Missing Values in a Pareto Genetic Algorithm Used in Parameter Design. *Ingeniería e Investigación, 37* (2), 89–98.
22. Bentouati, B., Chettih, S., & Esehiemi, R. (2017). A Chaotic Firefly Algorithm for Non-convex Economic Dispatch Problem. *Electrotehnica, Electronica, Automatica (EEA), 60* (1), 172–179. ISSN 1582-5175.
23. Eiben, A.E., & Smith, J.E. (2015). *Introduction to Evolutionary Computing* (2nd ed.) Berlin: Springer Verlag, Heidelberg.
24. Zhang, Y., & Zhou, D. (2016). Application of differential evolution algorithm in future collider optimization. In: Proceedings of IPAC'16 (pp. 2–4). 8–13 May 2016, BEXCO, Busan Korea.
25. Zhao, J., Li, T., & Ian, J. (2005). Application of particle swarm optimization algorithm on robust PID controller tuning. In: Advances in Natural Computation (ICNC). 27–29 August 2005, Changsha, China. Heidelberg: Springer-Verlag Berlin.
26. Karaboga, D., & Okdem. S. (2016). A Modified Artificial Bee Colony (ABC) Algorithm for Constrained Optimization Problems. *Applied Soft Computing, 11* (3), 3021–3031.

27. Sheikholeslami, R., & Kaveh, A. (2013). A Survey of Chaos Embedded Meta-Heuristic Algorithms. *Int. J. Optim. Civil. Eng., 3* (4), 617–633.

28. Wen, H., Hou, S., Liu, Z., & Liu, Y. (2017). An Optimization Algorithm for Integrated Remanufacturing Production Planning and Scheduling System. *Chaos, Solutions & Fractals, 105*, 69–76.